



1 **ENSO Modulation of the QBO Periods in GISS E2.2 Models**

2 Tiehan Zhou^{1,2}, Kevin J. DallaSanta^{1,3}, Clara Orbe^{1,3}, David H. Rind¹, Jeffrey A. Jonas^{1,2},

3 Larissa Nazarenko^{1,2}, Gavin A. Schmidt¹, Gary Russell¹

4

5 ¹NASA Goddard Institute for Space Studies, New York, NY

6 ²Center for Climate Systems Research, Columbia University, New York, NY

7 ³Department of Applied Physics and Applied Mathematics, Columbia University, New York, NY

8

9 Correspondence to: Tiehan Zhou (tz2131@columbia.edu)

10

11 **Abstract.** Observational studies have shown that the El Niño–Southern Oscillation (ENSO) exerts
12 an influence on the Quasi-Biennial Oscillation (QBO). The downward propagation of the QBO tends to
13 speed up and slow down during El Niño and La Niña, respectively. Recent results from general
14 circulation models have indicated that the ENSO modulation of the QBO requires a relatively high
15 horizontal resolution, and that it does not show up in the climate models with parameterized but
16 temporally constant gravity wave sources. Here, we demonstrate that the NASA GISS E2.2 models can
17 capture the observed ENSO modulation of the QBO period with a horizontal resolution of 2° latitude by
18 2.5° longitude and its gravity wave sources parameterized interactively. This is because El Niño events
19 lead to more vigorous gravity wave sources generating more absolute momentum fluxes over the
20 equatorial belt, as well as less filtering of these waves into the tropical lower stratosphere through a
21 weakening of the Walker circulation. Various components of the ENSO system such as the SSTs, the
22 convective activities, and the Walker circulation are intimately involved in the generation and
23 propagation of parameterized gravity waves, through which ENSO modulates the QBO period in GISS
24 E2.2 models.



25

26 **1. Introduction**

27 The QBO dominates the interannual variability in the tropical stratosphere (Baldwin et al., 2001)
28 while ENSO is the primary mode of interseasonal–interannual variability over the tropical Pacific Ocean
29 (Wang et al., 2016). It is well-known that both the QBO and the ENSO have far-reaching implications
30 for global weather and climate systems (Hamilton et al., 2015; Philander, 1990; Domeisen et al., 2019).

31 The QBO and the ENSO defy linear relationships (Angell, 1986; Xu, 1992; Garfinkel and Hartmann,
32 2007). However, Maruyama and Tsuneoka (1988) spotted an intriguing connection between the
33 anomalously short easterly phase of the QBO at 50 hPa in 1987 and the El Niño event that persisted
34 through that year. Based on the results from a mechanistic model, Geller et. al (1997) suggested that the
35 equatorial sea surface temperatures (SST) modulate the wave momentum fluxes into the stratosphere
36 and thus the QBO. Remarkably, an observational study conducted by Taguchi (2010) demonstrated that
37 the downward propagation of the QBO tends to speed up during El Niño and slow down during La Niña
38 while the amplitude of the QBO tends to be smaller during El Niño and larger during La Niña,
39 respectively. Using radiosonde data from 10 near-equatorial stations distributed along the Equator, Yuan
40 et al. (2014) found that the ENSO modulation of the QBO period is more robust than that of the QBO
41 amplitude.

42 The QBO influences the distribution and transport of various chemical constituents (Zawodny and
43 McCormick, 1991; Trepte and Hitchman, 1992; Hasebe, 1994; Kawatani et al., 2014), the extratropical
44 circulation in the winter stratosphere (Holton and Tan, 1980; Labitzke, 1982), tropical moist convection
45 (Collimore et al., 2003; Liess and Geller, 2012), the activities of tropical cyclones (Gray et al., 1984; Ho
46 et al., 2009), the ENSO (Gray et al., 1992; Huang et al., 2012; Hansen et al. 2016), the Hadley circulation
47 (Hitchman and Huesmann, 2009), the tropospheric subtropical jet (Garfinkel and Hartmann, 2011a,



48 2011b), the boreal summer monsoon (Giorgetta et al., 1999), and the Madden-Julian Oscillation (Yoo
49 and Son, 2016). Thus, it is imperative that weather and climate models have the capacity to simulate the
50 ENSO modulation of the QBO.

51 Schirber (2015) conducted two sets of experiments to explore this issue using the general circulation
52 model European Centre/Hamburg 6 (ECHAM6) wherein a convection-based gravity wave scheme was
53 newly implemented. The first set of experiments was called QBOW where the initial QBO
54 configurations consisted of a westerly jet above the 10 hPa level and an easterly jet below that level.
55 Likewise, in the second set of experiments named as QBOE, the initial QBO conditions included an
56 easterly and westerly jet above and below the 10 hPa level, respectively. Schirber showed that for QBOW,
57 the ensemble mean period of the QBO from the El Niño runs is shorter than that from the La Niña runs
58 while for QBOE, the ensemble mean periods are comparable between the El Niño and the La Niña runs.
59 He also noted that there is no systematic change in amplitude of the QBO jets between El Niño and La
60 Niña runs. Using version 3 of the EC-Earth Consortium's climate model with its horizontal resolution
61 of T255 spectral truncation, Christiansen et al. (2016) reported that all ensemble members had a faster
62 QBO descent rate during El Niño than during La Niña, and that their ensemble mean QBO phase speeds
63 were comparable to those derived from the reanalyses.

64 Employing two atmospheric general circulation models (AGCM) developed under the Model for
65 Interdisciplinary Research on Climate (MIROC) framework, Kawatani et al. (2019) investigated the
66 possible mechanism of the ENSO modulation of the QBO. They first compared a 100-year perpetual El
67 Niño run with a 100-year perpetual La Niña run from the MIROC-AGCM with T106 horizontal
68 resolution and 500-m vertical spacing in the stratosphere without any nonorographic gravity wave
69 parameterizations. Then they repeated the two AMIP-style perpetual El Niño and La Niña experiments
70 but using the atmospheric part of the Model for Interdisciplinary Research on Climate, Earth System



71 Model (MIROC-ESM) with T42 horizontal resolution and 700-m vertical spacing in the stratosphere
72 where the effects of nonorographic gravity waves are parameterized and the gravity wave sources are
73 held constant in time. They found that the MIROC-AGCM simulates shorter QBO periods during El
74 Niño than during La Niña because of the larger equatorial vertical wave fluxes of zonal momentum in
75 the uppermost troposphere and consequently the much larger resolved gravity wave forcing in the
76 stratosphere during warm ENSO phase. However, they found almost no difference in the average QBO
77 periods simulated by the MIROC-ESM between El Niño and La Niña because the QBO was generated
78 by the parameterized nonorographic gravity wave forcing in the model where the gravity wave sources
79 were held constant in time, thus did not respond to the SST changes associated with the ENSO cycle.

80 Serva et al. (2020) found that a relatively high horizontal resolution was necessary to simulate the
81 observed modulation of the QBO descent rate under strong ENSO events, while the amplitude response
82 is generally weak at any horizontal resolution. They also pointed out that over-dependence on
83 parameterizing the effects of gravity waves with temporally invariant sources is detrimental to the
84 realistic simulation of the coupling between the ocean and the tropical stratosphere in current climate
85 models.

86 As far as the ENSO modulation of the QBO period is concerned, both Kawatani et al. (2019) and
87 Serva et al. (2020) emphasized the importance of a relatively high horizontal resolution and the
88 inadequacy of non-interactive gravity wave sources. However, the exploratory work of Schirber (2015)
89 shows that the ENSO modulation of the QBO period can, to some extent, be simulated in the GCM
90 ECHAM6 with T63 and an associated Gaussian grid of $\sim 1.9^\circ$ horizontal resolution because rather than
91 being held constant in time, the properties of non-interactive gravity wave sources in the tropics are
92 determined by the simulated convection which is modulated by ENSO phases.



93 Rind et al. (1988) pioneered the use of meteorologically interactive gravity wave sources in the
94 Goddard Institute for Space Studies (GISS) climate models. By increasing the vertical resolution and
95 revising the formulations, various versions of the GISS models subsequently simulate a spontaneous
96 QBO (Rind et al., 2014, 2020; DallaSanta et al., 2021). The GISS E2.2 models are comprehensive
97 climate models optimized for the middle atmosphere (Rind et al., 2020; Orbe et al., 2020). Their outputs
98 have been submitted to the archive of the Coupled Model Intercomparison Project Phase 6 (CMIP6).
99 Bushell et al. (2020) pointed out that most of current climate models are highly dependent on
100 parameterized nonorographic gravity wave forcing to simulate a QBO. Unsurprisingly, DallaSanta et al.
101 (2021) found that the parameterized convective gravity waves play a dominant role in generating the
102 spontaneous QBO in the GISS E2.2 models.

103 In this paper, we will compare the QBO simulated by the GISS E2.2 models with observations and
104 investigate how the ENSO modulates the QBO period in those models. Section 2 revisits the ENSO
105 modulation of the QBO from the observational point of view. Section 3 evaluates the ENSO modulation
106 of QBO period in the historical runs simulated by five versions of the GISS E2.2 models. Section 4
107 explores the physical mechanisms underlying the simulated modulation. Conclusions and discussion are
108 presented in section 5.

109

110 **2. Revisiting the ENSO modulation of the QBO from observations**

111 **2.1 Observations**

112 Before evaluating the GISS E2.2 models, we first follow Taguchi (2010) to revisit the ENSO
113 modulation of the QBO from the observational point of view.

114 The monthly mean zonal winds are provided by Free University of Berlin (FUB). The FUB data were
115 produced by combining the radiosonde observations at the following three equatorial stations: Canton



116 Island near 172°W, 3°S (closed in 1967), Gan/Malediva Islands near 73°E, 1°S (closed in 1975), and
117 Singapore near 104°E, 1°N (Naujokat, 1986). We use 63 years (i.e., 756 months) of the FUB data ranging
118 from 1953 to 2015 at the following seven pressure levels: 70, 50, 40, 30, 20, 15, and 10 hPa. As in
119 Taguchi (2010), we first fill the missing zonal winds at the 10 hPa level for the first 3 years by linear
120 extrapolation in log-pressure height, and then remove the climatological seasonal cycle from the data for
121 each calendar month. We further smooth the deseasonalized zonal winds using a 5-month moving
122 average (for more details, refer to Taguchi, 2010).

123 The National Oceanic and Atmospheric Administration (NOAA) Extended Reconstructed SST
124 (ERSST) V5 datasets (Huang et al., 2017) are provided by National Centers for Environmental
125 Information (NCEI). ERSST produced on a $2^\circ \times 2^\circ$ grid is derived from the International
126 Comprehensive Ocean-Atmosphere Data Set (ICOADS). The latest version of ERSST, version 5, uses
127 new datasets from ICOADS Release 3.0 SST, combining information from Argo floats above 5 m and
128 Hadley Centre Ice-SST version 2 ice concentrations. In addition, the monthly Outgoing Longwave
129 Radiation (OLR) on a $2.5^\circ \times 2.5^\circ$ grid is provided by NCEI for the 1979–2015 period. We use the OLR
130 values as a proxy for tropical convection since cloud top temperatures are negatively correlated with
131 cloud height in the tropics.

132 We use the ERSSTv5 data to construct the Oceanic Niño Index (ONI) ranging from 1953 to 2015.
133 We use the same method to calculate the ONI as the Climate Prediction Center (CPC) of NOAA. Namely,
134 the ONI is defined as a 3-month running mean of ERSSTv5 SST anomalies in the Niño 3.4 region
135 ($5^\circ\text{S} - 5^\circ\text{N}$, $120^\circ - 170^\circ\text{W}$) based on centered 30-year base periods updated every 5 years
136 (https://origin.cpc.ncep.noaa.gov/products/analysis_monitoring/ensostuff/ONI_v5.php). This method
137 ensures a proper identification of El Niño and La Niña by taking the secular changes in SSTs into account.
138 The SST anomalies are defined as the deviations of the SST from its climatological annual cycle over a



139 selected base period. Specifically, the SST anomalies during 1951–1955 are based on the 1936–1965
140 base period; the SST anomalies during 1956–1960 are based on the 1941–1970 base period; and so on.
141 Thus, as the CPC of NOAA we used the ERSSTv5 SST from January 1936 to January 2016 period to
142 obtain the ONI from January 1953 to December 2015.

143 Following the CDC of NOAA, we refer to El Niño or La Niña episodes as the periods when the ONIs
144 are greater than $+0.5^{\circ}\text{C}$ or less than -0.5°C for at least five consecutive months, respectively. We will
145 use this same criterion to identify El Niño and La Niña events simulated by the GISS E2.2 models in
146 section 3. Since the temperature measurement is only accurate to the tenths place, all our calculated ONIs
147 are rounded to the nearest tenth. Based on the rounded ONIs, our identified El Niño and La Niña episodes
148 are almost identical to those listed at the abovementioned website of NOAA CPC. Accordingly, we
149 identified 21 El Niño and 15 La Niña events between 1953 and 2015.

150 **2.2 ENSO modulation of the QBO derived from observations**

151 Following Wallace et al. (1993), we decompose the deseasonalized and smoothed FUB zonal winds
152 from 10 to 70 hPa into two leading pairs of empirical orthogonal functions (EOFs) and principal
153 components (PCs) because they typically account for more than 90% of the vertical structure variance
154 (Wallace et al., 1993; DallaSanta et al., 2021). For the sake of robustness, we exclude the FUB data after
155 2015 as the first two EOFs explain no more than 60% of total variance during the 2016 and 2019/20
156 QBO disruptions (Anstey et al., 2021).

157 Fig. 1 depicts the two leading EOFs derived from the deseasonalized and smoothed FUB zonal winds
158 between 1953 and 2015. The vertical structures of those two EOFs are very similar to those depicted in
159 Fig. 2a of Taguchi (2010) who used the FUB zonal winds from 1953 to 2008. Our calculated two leading
160 EOFs account for 95.9% of the vertical structure variance (59.6% by EOF1 and 36.3% by EOF2) which
161 is very close to the value of 96.1% obtained by Taguchi (2010). Thus, the QBO variability can be, to a



162 very good approximation, compactly depicted by the trajectory of $(PC_1(t), PC_2(t))$ in a linear space
163 spanned by the first two orthonormal EOFs.

164 Following previous studies (Wallace et al., 1993; Taguchi, 2010, Christiansen et al. 2016; Serva et al.
165 2020; DallaSanta et al., 2021), the instantaneous amplitude (A) and phase (ψ) of the QBO are defined
166 as

$$167 \quad A = \sqrt{PC_1^2 + PC_2^2} \quad (1)$$

$$168 \quad \psi = \text{atan2}(PC_2, PC_1) \quad (2)$$

169 Differentiating (2) with respect to time yields the instantaneous phase speed of the QBO:

$$170 \quad \psi' = (PC_1 \cdot PC_2' - PC_1' \cdot PC_2) / (PC_1^2 + PC_2^2) \quad (3)$$

171 Now we have two sample spaces: one consists of 21 independent El Niño events and the other
172 contains 15 independent La Niña events. For each ENSO event, we define the amplitude and phase speed
173 (Ψ') of the QBO as the values of A in Eq. (1) and ψ' in Eq. (3) that are averaged over the number of
174 months of that event. Thus, two random variables A and Ψ' , i.e., the amplitude and phase speed of the
175 QBO, are defined both on the El Niño sample space and on the La Niña sample space. We employ
176 Welch's t -test (Moser and Stevens, 1992) to examine whether there is a significant difference in A or Ψ'
177 between the El Niño and La Niña population means.

178 To examine whether the sample mean QBO amplitude is significantly different between El Niño and
179 La Niña, we first construct the statistic:

$$180 \quad t = \frac{\bar{A}_1 - \bar{A}_2}{S_{\bar{A}_1 - \bar{A}_2}} \quad (4)$$

181 where \bar{A}_1 and \bar{A}_2 are the sample mean A for El Niño and La Niña episodes, respectively.

$$182 \quad S_{\bar{A}_1 - \bar{A}_2} = \sqrt{\frac{s_{A_1}^2}{N_1} + \frac{s_{A_2}^2}{N_2}} \quad (5)$$



183 where s_{A_1} and s_{A_2} are the corrected sample standard deviation of A for El Niño and La Niña,
184 respectively while N_1 and N_2 are the sample sizes of El Niño and La Niña events. According to Moser
185 and Stevens (1992), the degrees of freedom for the t -distribution is

$$186 \quad \nu = \frac{\left(s_{A_1}^2/N_1 + s_{A_2}^2/N_2\right)^2}{\left(\frac{s_{A_1}^2}{N_1}\right)^2 / (N_1 - 1) + \left(\frac{s_{A_2}^2}{N_2}\right)^2 / (N_2 - 1)} \quad (6)$$

187 As mentioned before, there are 21 El Niño and 15 La Niña episodes between 1953 and 2015, i.e.,
188 $N_1 = 21$ and $N_2 = 15$. Our calculations yield $\bar{A}_1 = 37.2 \text{ ms}^{-1}$, $\bar{A}_2 = 40.6 \text{ ms}^{-1}$, $\nu = 33$, and $t =$
189 -2.01 . Apparently, $\bar{A}_1 < \bar{A}_2$, which suggests that the QBO amplitude is smaller during El Niño than
190 during La Niña. Performing a two-tailed test with $\nu = 33$ and $t = -2.01$, however, we find that the
191 QBO amplitudes during El Niño episodes are not statistically different from those during La Niña
192 episodes at the 5% significance level. This is consistent with the finding of the observational study by
193 Yuan et al. (2014), namely, the ENSO modulation of the QBO amplitude is less robust than that of the
194 QBO period. This is also consistent with the findings of the modeling studies conducted by Schirber
195 (2015) and Serva (2020).

196 Note that when we use the FUB zonal winds and the ERSSTv5 data over the 1953–2008 period as
197 Taguchi (2010), our calculations yield $N_1 = 19$, $N_2 = 13$, $\bar{A}_1 = 36.7 \text{ ms}^{-1}$, $\bar{A}_2 = 41.5 \text{ ms}^{-1}$, $\nu = 30$,
198 and $t = -3.23$. A two-tailed test shows that the difference of the QBO amplitude between El Niño and
199 La Niña is statistically significant at the 1% significance level. Note that most data used by Yuan et al.
200 (2014) ended in 2011. The sample sizes of the El Niño and La Niña events are relatively small since
201 1953 when the equatorial zonal winds began to be available. Since the results of various studies are
202 sensitive to how the available data are selected, we will not further explore in this study whether the
203 ENSO modulates the QBO amplitude for the sake of robustness.



204 To examine whether the sample mean QBO phase speed is significantly different between El Niño
205 and La Niña, we similarly use Eqs. (4) – (6) except that A_1 and A_2 are replaced by Ψ'_1 and Ψ'_2 ,
206 respectively. Based on the data from 1953 to 2015, our calculations yield $N_1 = 21$ and $N_2 = 15$, $\overline{\Psi'_1} =$
207 0.244 radians/month, $\overline{\Psi'_2} = 0.186$ radians/month, $\nu = 28$, and $t = 2.47$. Evidently, $\overline{\Psi'_1} > \overline{\Psi'_2}$,
208 indicating that the phase speed of the QBO is greater during El Niño than during La Niña. Performing a
209 two-tailed test with $\nu = 28$ and $t = 2.47$, we ascertain that the phase speed of QBO during El Niño
210 episodes are statistically different from those during La Niña episodes at the 5% significance level. Put
211 in another way, the mean QBO period of 25.8 months (i.e., $2\pi/0.244$) during El Niño is statistically
212 shorter than that of 33.8 months (i.e., $2\pi/0.186$) during La Niña. Furthermore, when we use the FUB
213 zonal winds and the ERSSTv5 data over the 1953–2008 period as Taguchi (2010), our calculations yield
214 $N_1 = 19$ and $N_2 = 13$, $\overline{\Psi'_1} = 0.250$ radians/month, $\overline{\Psi'_2} = 0.182$ radians/month, $\nu = 25$, and $t = 2.83$.
215 Apparently, we reach a similar conclusion that the mean QBO period of 25.1 months (i.e., $2\pi/0.250$)
216 during El Niño is statistically shorter than that of 34.5 months (i.e., $2\pi/0.182$) during La Niña. Since
217 our conclusion is consistent with that of Taguchi (2010), we regard it robust that the QBO descent is
218 faster during El Niño than during La Niña. Henceforth, we will focus only on the ENSO modulation of
219 the QBO period in this study.

220 To facilitate comparison with other studies (e.g., Taguchi, 2010; Christiansen et al., 2016; Serva et
221 al. 2020), we also calculate the mean phase speed of the QBO by averaging ψ' in Eq. (3) over all the
222 210 months of the El Niño episodes and over all the 201 months of the La Niña episodes between 1953
223 and 2015. Subsequently, we obtain the mean QBO period of 25.9 months during El Niño and of 32.0
224 months during La Niña for the 1953–2015 period. Similarly, we obtain the mean phase speed of the
225 QBO by averaging ψ' in Eq. (3) over all the 186 months of the El Niño episodes and over all the 174
226 months of the La Niña episodes for the 1953–2008 period. The resultant values are 25.3 and 32.0 months,



227 respectively, which are very close to 25 and 32 months inferred by Taguchi (2010). No matter whether
228 the selected FUB data span from 1953 to 2008 or range from 1953 to 2015, we robustly conclude that
229 the QBO descent rate is faster during El Niño than during La Niña.

230 Note that it is difficult to rigorously determine the degrees of freedom for a t -test when we choose the
231 monthly data as sample points which share some common characteristics, i.e., are not independent of
232 each other during an ENSO event (for more details, refer to Taguchi, 2010). In the remaining of this
233 paper, when we need to conduct a Welch's t -test we choose the QBO period averaged over each ENSO
234 episode as a sample point. Otherwise, the mean values during El Niño or La Niña are referred to the
235 quantities averaged over all the months of El Niño or La Niña category in alignment with previous works
236 conducted by Taguchi (2010), Christiansen et al. (2016), and Serva et al. (2020).

237 The QBO is mainly driven by tropical waves (Lindzen and Holton, 1968; Holton and Lindzen, 1972;
238 Plumb 1977) of which tropical convection is an important source (Holton, 1972; Salby and Garcia, 1987;
239 Bergman and Salby, 1994; Tsuda et al., 2009; Alexander et al., 2017). To investigate how tropical
240 convection is influenced by the ENSO, we first produce the monthly OLR anomalies ranging from 1979
241 to 2015 by deseasonalizing the monthly OLR data downloaded from the website of NOAA NCEI. Then
242 we obtain the mean OLR anomalies for La Niña and El Niño conditions by averaging the monthly OLR
243 anomalies over all the months that fall into La Niña and El Niño categories, respectively. Fig. 2a show
244 that mean OLR anomalies exhibit a broad and positive pattern that spans the central and eastern
245 equatorial Pacific and a negative pattern in the maritime continent for the La Niña conditions. In contrast,
246 Fig. 2b show that they exhibit a broad and negative pattern that spans the central and eastern equatorial
247 Pacific and a positive pattern in the maritime continent for the El Niño conditions. The large differences
248 in the mean OLR anomalies in Fig. 2c between El Niño and La Niña conditions are closely related with
249 the contrast in the SST anomalies patterns shown in Fig. 3. Namely, the distinctive patterns of positive



250 and negative SST anomalies extend over the central and eastern Pacific during the El Niño and La Niña
251 episodes, respectively, which not only gives rise to the corresponding positive and negative rainfall
252 anomalies (Philander, 1990) and the concomitant OLR anomalies shown in Fig. 2, but also leads to
253 various teleconnections outside the tropics (Domeisen et al., 2019).

254 In the next section, we will evaluate how the ENSO modulates of the QBO periods in the E2.2 models
255 and whether those models can realistically capture the contrast in the OLR patterns that generally
256 underlies the difference in wave driving of the QBO between warm and cold ENSO conditions.

257

258 **3. ENSO modulation of the QBO period in GISS E2.2 models**

259 **3.1 Description of the models and simulations**

260 GISS E2.2 is a climate model specially optimized for the middle atmosphere (Rind et al., 2020; Orbe
261 et al., 2020) and its output was submitted to the Coupled Model Intercomparison Project Phase 6 (CMIP6)
262 archive. The horizontal resolution of all GISS E2.2 models is 2° (latitude) \times 2.5° (longitude) for the
263 atmosphere and the model extends from the surface to 0.002 hPa (\sim 89 km) with 102 vertical layers (for
264 more details, see Table 1 in Rind et al., 2020). Note that an adequate vertical resolution is necessary for
265 climate models to internally generate a spontaneous QBO (Scaife et al., 2000; Richter et al. 2014; Rind
266 et al, 2014, 2020; Geller et al. 2016a; Butchart et al. 2018).

267 According to composition interactivity, the atmospheric component of the GISS E2.2 models was
268 configured in two ways for CMIP6. The first configuration is denoted as NonINTeractive (“NINT”)
269 where the fields of radiatively active components such as ozone and multiple aerosol species are
270 specified from previously calculated offline fields (Kelley et al. 2020; Miller et al., 2021). The second
271 configuration includes interactive gas-phase chemistry and a mass-based (One-Moment Aerosol, OMA)
272 aerosol module, where aerosols and ozone are driven by emissions and calculated prognostically (Bauer



273 et al., 2020; Nazarenko et al., 2022). The abovementioned NINT and OMA configurations correspond
274 to physics-version=1 (“p1”) and physics-version=3 (“p3”), respectively, in the CMIP6 archive.

275 The basic dynamics and tropospheric physics structure of the GISS E2.2 models were based on the
276 GISS E2.1 model (Kelley et al., 2020). One version of the cloud parameterization schemes used in E2.2,
277 termed as “standard physics” (SP), has not been fully upgraded to the state-of-the-art module customized
278 for E2.1 which has only 40 vertical layers up to 0.1 hPa (Rind et al., 2020). Accordingly, E2.2–SP has a
279 younger sibling, E2.2–AP, whose cloud parameterization schemes, termed as “Altered Physics” (AP),
280 are more aligned with those in E2.1 and whose outputs were thus favored for the submission to the
281 CMIP6 archive. “Altered Physics” in E2.2–AP brings about a somewhat different response to SST as
282 compared with the “standard physics” in E2.2–SP. Since the QBO in the GISS models are mainly driven
283 by gravity waves (DallaSanta et al., 2021) and the phase velocities and momentum fluxes of gravity
284 wave sources are coupled to convective cloud-top-pressure altitudes, convective mass fluxes,
285 background wind fields, etc. (Rind et al., 1988, 2014, 2020), both E2.2–SP and E2.2–AP are included in
286 this study to gain insight into the mechanisms through which ENSO modulates the QBO period despite
287 the fact that the outputs of E2.2–SP were not submitted to the CMIP6 archive. Note that outputs from
288 E2.2–SP models, following the CMIP6 protocol and naming, are available from NASA NCCS portal
289 (under the title E2.2.1).

290 Here we look into two atmosphere-only (AMIP) ensemble simulations where the evolution of SST
291 and sea ice fraction (SIF) is specified and three coupled ensembles where the respective model
292 atmosphere interacts with the ocean component termed as the GISS Ocean v1 (GO1) which extends from
293 the surface to the ocean floor with 40 vertical layers and has a horizontal resolution of 1° latitude by
294 1.25° longitude (Schmidt, et al., 2014; Kelley et al., 2020). Table 1 lists the five model configurations
295 and their respective ensemble simulations investigated in this study.



296 The first two ensembles in Table 1 were generated by AMIP–OMA–SP and AMIP–OMA–AP models
297 where the SST and SIF from the HadISST1 dataset (Rayner et al., 2003) were prescribed for the
298 simulations between 1870 and 2014 while their climatological annual cycles over the 1876–1885 period
299 were imposed for the earlier simulations between 1850 and 1869. Both AMIP–OMA–SP and AMIP–
300 OMA–AP prognostically calculate the concentrations of ozone, methane, chlorofluorocarbons, aerosols,
301 etc. AMIP–OMA–SP and AMIP–OMA–AP differ only in the package of cloud parameterization
302 schemes, which leads to their different responses to SST and thus may have important implications for
303 simulating the ENSO modulation of the QBO period. We discarded the simulations ranging from 1850
304 to 1869 in this study because they are irrelevant to the ENSO modulation of the QBO in the absence of
305 interannual variations in the prescribed SST over that period. Note that the two extended historical AMIP
306 simulations from 1870 to 2014 listed in Table 1 were not submitted to the CMIP6 archive. However,
307 AMIP–OMA–AP did generate a 5-member ensemble over the 1979–2014 period that was submitted to
308 the CMIP6 archive and tagged as E2-2-G.amip.r[1-5]i1p3f1. It is worth noting that the climatological
309 characteristics over the 1979–2014 period derived from the AMIP–OMA–AP ensemble listed in Table
310 1 should be comparable to those derived from E2-2-G.amip.r[1-5]i1p3f1 albeit the climate trajectories
311 of the individual ensemble members over the 1979–2014 period are expected to differ between those
312 two ensembles starting from January 1850 and January 1979, respectively, due to the chaotic nature of
313 climate systems.

314 The other three ensembles in Table 1 were generated by the Coupled–NINT–SP, Coupled–NINT–
315 AP, and Coupled–OMA–AP models where the respective atmospheric components are coupled with
316 GO1. Both the Coupled–NINT–SP and Coupled–NINT–AP simulations were performed with the
317 prescribed atmospheric composition generated from the AMIP-style OMA simulations using the
318 historical forcings over the 1850–2014 period. As mentioned earlier with regard to the AMIP–OMA–SP



319 and AMIP–OMA–AP runs, the difference in cloud physics between the Coupled–NINT–SP and
320 Coupled–NINT–AP models is exploited to gain a deeper insight into the mechanisms through which the
321 ENSO modulates the QBO periods. Coupled–OMA–AP, the last of the abovementioned three ensembles,
322 is computationally expensive because not only the atmosphere and ocean interact with each other but
323 also the radiative, dynamical, and chemical processes are coupled to each other. All three coupled runs
324 started from January 1850 and ended in December 2014.

325 **3.2 ENSO modulation of the QBO period derived from the ensemble simulations**

326 Now we investigate the ENSO modulation of the QBO period in the ensemble simulations listed in
327 Table 1. As mentioned in the preceding subsection, there are no interannual variations in the prescribed
328 SST over the 1850–1869 period for both the AMIP–OMA–SP and AMIP–OMA–AP runs. Thus, our
329 analyses focus on the 1870–2014 period for those two ensembles. For the sake of conciseness and
330 consistency, we also discarded the outputs from three coupled runs over the 1850–1869 period. In short,
331 we only analyze the data over the 1870–2014 period from the ensemble simulations listed in Table 1.

332 Following section 2, we define the ONI as a 3-month running mean of either prescribed SST
333 anomalies from the AMIP–OMA–SP or AMIP–OMA–AP runs or simulated SST anomalies from the
334 Coupled–NINT–SP, Coupled–NINT–AP, and Coupled–OMA–AP runs in the Niño 3.4 region (5°S– 5°N,
335 120°– 170°W) based on centered 30-year base periods updated every 5 years. This method can properly
336 identify El Niño and La Niña by removing the secular changes in SSTs. As in section 2, the SST
337 anomalies are defined as the deviations of the SST from its climatological annual cycle over a selected
338 base period. Specifically, the SST anomalies during 1886–1890 are based on the 1871–1900 base period;
339 the SST anomalies during 1891–1895 are based on the 1876–1905 base period; the SST anomalies during
340 1991–1995 are based on the 1976–2005 base period; the SST anomalies during 1996–2000 are based on
341 the 1981–2010 base period. In addition, the SST anomalies during the earliest 1870–1885 and latest



342 2011–2014 spans are ad hoc based on the 1870–1899 and 1985–2014 base periods, respectively. Thus,
343 we used the specified or simulated SSTs over the 1870–2014 period to obtain the ONI from February
344 1870 to November 2014. For convenience and conciseness, we will only explore the ENSO influence
345 on the QBO period over the 1871–2013 time span in this study.

346 To obtain the QBO winds from the ensemble simulations listed in Table 1, we first calculate the zonal
347 mean monthly mean zonal winds averaged from 5° S to 5° N over the 1871 to 2013 period at the
348 following seven pressure levels: 70, 50, 40, 30, 20, 15, and 10 hPa. Then we remove the climatological
349 seasonal cycle from the equatorial zonal mean monthly mean zonal winds at each of those seven levels
350 for each calendar month. We further smooth the deseasonalized data using a 5-month moving average
351 following Taguchi (2010) and section 2.

352 As in section 2, we decompose the QBO winds from 10 to 70 hPa over the 1871–2013 period into
353 two leading pairs of empirical orthogonal functions (EOFs) and principal components (PCs). For each
354 of the 24 ensemble simulations listed in Table 1, the first two leading EOFs account for at least 92.9%
355 of the vertical structure variance which is slightly smaller than the value of 95.9% derived from the
356 observations discussed in section 2. Fig. 4 depicts the first two leading EOFs from each of all five
357 Coupled–NINT–AP runs. For each of those five runs, the first two leading EOFs account for at least
358 93.8% of the vertical structure variance. The vertical structures of those two EOFs from each Coupled–
359 NINT–AP run are broadly similar to those derived from observations in Fig. 1. The respective vertical
360 structures of the first two leading EOFs are almost identical among all five Coupled–NINT–AP ensemble
361 runs, which is expected because all runs share the same model and differ from each other only in their
362 initial conditions. It is worth noting that the vertical structures of the first two leading EOFs shown in
363 Fig. 4 somewhat differ from those shown in Fig. 1 below the 20 hPa level because none of CMIP models
364 could simulate a QBO in the lower stratosphere that is as strong as the observed (Richter et al., 2020).



365 In addition, we find that the vertical structures of the first two leading EOFs from other four ensemble
366 simulations listed in Table 1 (figures not shown) are comparable to those from the Coupled-NINT-AP
367 runs. Thus, the simulated QBO variabilities in each ensemble can be, to a very good approximation,
368 compactly depicted by the trajectory of $(PC_1(t), PC_2(t))$ in a linear space spanned by the first two
369 orthonormal EOFs.

370 For the ensemble simulations listed in Table 1, we define an El Niño or La Niña event in the same
371 way as we did in section 2. Similarly, Eq. (3) is used to calculate the instantaneous (i.e., monthly) phase
372 speed of the simulated QBO. For each El Niño or La Niña event, the mean phase speed of the simulated
373 QBO from any individual run listed in Table 1 is obtained by averaging the instantaneous phase speeds
374 of the simulated QBO over the number of months of that event. Accordingly, we have one sample space
375 consisting of independent El Niño events and the other consisting of independent La Niña events. As in
376 section 2, we employ a two-tailed Welch's *t*-test to examine whether there is a significant difference in
377 the phase speed of the simulated QBO between the El Niño and La Niña population means.

378 Table 2 describes how the ENSO influence the QBO period in each member of all ensembles, where
379 E[1-5] represent AMIP-OMA-SP, AMIP-OMA-AP, Coupled-NINT-SP, Coupled-NINT-AP, and
380 Coupled-OMA-AP ensembles, respectively while r_1, r_2, \dots indicate its respective member of each
381 ensemble. For the member r_1 of E1, i.e., the first run of the AMIP-OMA-SP ensemble, we identified
382 34 El Niño and 30 La Niña events between 1871 and 2013, i.e., $N_1 = 34$ and $N_2 = 30$ in Eqs. (5) and
383 (6). Then we obtained the phase speed of the QBO for each episode of those 34 El Niño and 30 La Niña
384 events, from which we derived the mean phase speed of the QBO averaged over the 34 El Niño and 30
385 La Niña events, respectively. Accordingly, our mean phase speeds of the QBO simulated by r_1 of E1
386 averaged over the El Niño and La Niña events are obtained as 0.202 radians/month and 0.185
387 radians/month, respectively, and the standard deviations about those mean phase speeds as 0.0345



388 radians/month and 0.0275 radians/month, respectively. Substituting those numbers into Eqs. (4) – (6)
389 yields $\nu = 61$, and $t = 2.25$. Therefore, the phase speed of the QBO simulated by r1 of E1 is statistically
390 significantly greater during El Niño than during La Niña at the 5% significance level. Accordingly, we
391 register the mean QBO period of 31.1 months (i.e., $2\pi/0.202$) during the El Niño episodes and 34.0
392 months (i.e., $2\pi/0.185$) during the La Niña episodes as the entries for r1 of E1 in Table 2. Since the
393 phase speeds of the QBO simulated by r1 of E1 are statistically significantly different between the El
394 Niño and La Niña categories at the 5% significance level, we can regard the QBO periods as being
395 statistically significantly different between El Niño and La Niña episodes and register their difference, -
396 2.9 months, in Table 2 with red and bold indicating this significance. Similarly, we calculated the QBO
397 periods during ENSO extremes and their difference simulated by every member of all ensembles and
398 registered them in Table 2 where the red and bold numbers indicate that the phase speed of the simulated
399 QBO is statistically significantly greater during El Niño than during La Niña at the 5% significance level.

400 Table 2 shows that 23 of 24 runs from the five GISS E2.2 models listed in Table 1 can simulate the
401 ENSO modulation of the QBO period discussed in section 2. For each member of the Coupled–NINT–
402 AP and Coupled–OMA–AP ensemble runs, the phase speed of the simulated QBO is statistically
403 significantly greater during El Niño than during La Niña at the 5% significance level. For the AMIP–
404 OMA–SP and AMIP–OMA–AP ensembles, most members also generate a spontaneous QBO whose
405 phase speed is statistically significantly greater during El Niño than during La Niña at the 5%
406 significance level. Intriguingly, in none of the Coupled–NINT–SP ensemble runs, the phase speed of the
407 simulated QBO is statistically significantly different between El Niño and La Niña episodes at the 5%
408 significance level albeit the contrast in the QBO periods between the two categories simulated by r1 of
409 E3 (i.e., Coupled–NINT–SP) is equal to -6.2 months and greater than that simulated by most members
410 of Coupled–NINT–AP and Coupled–OMA–AP. We will further look into this issue in section 5.



411 **4. Mechanisms of the ENSO modulation of the QBO period in GISS E2.2 models**

412 **4.1 ENSO modulation of the QBO forcings**

413 The QBO owes its existence to wave-mean flow interaction (Lindzen and Holton, 1968; Holton and
 414 Lindzen, 1972; Plumb, 1977). The evolution of zonal mean zonal winds is governed by the transformed-
 415 Eulerian-mean (TEM) momentum equation formulated in pressure coordinates on a sphere (Andrews et
 416 al., 1983):

$$417 \quad \frac{\partial \bar{u}}{\partial t} = \bar{G} + \frac{1}{\rho_0 a \cos \varphi} \bar{\nabla} \cdot \bar{F} - \left\{ \frac{\bar{v}^*}{a \cos \varphi} \left[\frac{\partial}{\partial \varphi} (\bar{u} \cos \varphi) - f \right] + \bar{\omega}^* \frac{\partial \bar{u}}{\partial p} \right\} + \bar{X}, \quad (7)$$

418 where the Eliassen-Palm flux \bar{F} is defined as

$$419 \quad \bar{F} = \{F^{(\varphi)}, F^{(p)}\} = a \cos \varphi \{ -\overline{u'v'} + \psi \bar{u}_p, -\overline{u'\omega'} - \psi [(a \cos \varphi)^{-1} (\bar{u} \cos \varphi)_\varphi - f] \}, \quad (8)$$

420 and its divergence as

$$421 \quad \bar{\nabla} \cdot \bar{F} = \frac{1}{a \cos \varphi} \frac{\partial}{\partial \varphi} (F^{(\varphi)} \cos \varphi) + \frac{\partial F^{(p)}}{\partial p}. \quad (9)$$

422 In Eq. (7), t denotes time, p pressure, φ latitude, (u, v, ω) "velocity" in (longitude, latitude, pressure)
 423 coordinates, a the mean radius of Earth, ρ_0 pressure-dependent basic density, and f the Coriolis
 424 parameter. In Eq. (8), ψ is defined as

$$425 \quad \psi = \overline{v'\theta'}/\bar{\theta}_p = -\overline{v'T'}/\left(\frac{\kappa \bar{T}}{p} - \frac{\partial \bar{T}}{\partial p}\right), \quad (10)$$

426 where θ denotes potential temperature, T temperature, and κ the ratio of the gas constant to the specific
 427 heat at constant pressure. Note that in Eqs. (7) – (10) primes denote departures from the zonal means
 428 which are represented by overbars, and residual meridional and vertical velocities, i.e., \bar{v}^* and $\bar{\omega}^*$, are
 429 defined as $(\bar{v} - \frac{\partial \psi}{\partial p})$ and $(\bar{\omega} + \frac{1}{a \cos \varphi} \frac{\partial (\psi \cos \varphi)}{\partial \varphi})$, respectively.



430 On the right hand side (RHS) of Eq. (7), the first term, \overline{G} , is the forcing from the gravity waves
431 parameterized in E2.2 models; the second term, $\frac{1}{\rho_0 a \cos \varphi} \vec{\nabla} \cdot \vec{F}$, is the forcing driven by the waves resolved
432 by GISS E2.2 models; the third term, $-\left\{ \frac{\vec{v}^*}{a \cos \varphi} \left[\frac{\partial}{\partial \varphi} (\overline{u} \cos \varphi) - f \right] + \overline{\omega}^* \frac{\partial \overline{u}}{\partial p} \right\}$, is associated with the TEM
433 advection; and last term, \overline{X} , is the zonal component of friction or other nonconservative mechanical
434 forcing (Andrew et al., 1987) that is small as far as the QBO is concerned and thus ignored in this study.

435 Section 3 shows that each historical simulation of the AMIP–OMA–SP, AMIP–OMA–AP, Coupled–
436 NINT–AP and Coupled–OMA–AP models brings about a faster downward propagation of the simulated
437 QBO during El Niño than during La Niña. The difference in the phase speed of the simulated QBO
438 between ENSO extremes is statistically significant at the 5% significance level for most of those model
439 runs. For Coupled–NINT–SP, one of its historical runs exhibits an opposite response, namely, the
440 simulated QBO propagates downward slower during El Niño than during La Niña while other four runs
441 of that model do bring about a faster phase speed of the QBO during warm ENSO events. However, no
442 matter whether the difference in the QBO period simulated by Coupled–NINT–SP is positive or negative
443 between ENSO extremes, it is not statistically significant at the 5% significance level. In this section,
444 we start with investigating how the first three terms in Eq. (7), i.e., the parameterized gravity wave
445 forcing, the resolved wave forcing, and the TEM advection, respond to ENSO extremes and how their
446 evolutions are related with those of the QBO winds simulated by the GISS E2.2 models.

447 As shown in sections 2 and 3, both the observed and simulated QBO can be very well represented by
448 the trajectory of $(PC_1(t), PC_2(t))$ in a linear space spanned by the first two orthonormal EOFs. In other
449 words, at any time t , the QBO wind profile, $U'_{profile}$ is very close to the following linear combination:
450 $PC_1(t) \cdot EOF_1 + PC_2(t) \cdot EOF_2$. Here, the QBO wind, U' , refers to the deseasonalized and smoothed
451 zonal mean monthly mean zonal winds averaged from 5° S to 5° N. We construct the composite fields



452 of the QBO winds, the gravity wave forcing, the resolved wave forcing, and the TEM advection
453 according to the phase angle of the QBO wind profiles. For each month that falls into the El Niño or La
454 Niña category, we use Eq. (2) to calculate the phase angle of the QBO wind profile, each cycle of which
455 over the 1871–2013 period is divided into 24 bins with the bin size of 15° . Note that if two QBO wind
456 profiles belong in the same bin, they look similar because any one of them can be expressed by the other
457 multiplied by a scalar factor. Therefore, for each of the El Niño and La Niña categories, it is very natural
458 for us to generate the composite QBO winds for that category by averaging all wind profiles in each bin
459 and produce the concomitant composite fields of the gravity wave forcing, the resolved wave forcing,
460 and the TEM advection in the corresponding bin.

461 Fig. 5 depicts the composite fields of the QBO winds (black contours) and parameterized (left panels)
462 and resolved (right panels) wave forcing averaged over all realizations of the Coupled–NINT–AP
463 ensemble. All composite fields in this section are the mean values over the 5°S – 5°N latitudes. The
464 ensemble average is achieved on the basis that the respective vertical structures of the first two leading
465 EOFs are almost identical among all five Coupled–NINT–AP ensemble runs as demonstrated in Fig. 4.
466 Both Figs. 5a and 5b show a characteristic feature of the QBO. Namely, the maximum eastward and
467 westward wave forcing from parameterized gravity waves are located below and propagate downward
468 with the westerly and easterly QBO jets. Fig. 5c reveals the stronger gravity wave forcing in both
469 eastward and westward shear zones of the QBO winds during El Niño than during La Niña, which gives
470 rise to the faster phase speed of the QBO during warm ENSO episodes than during its cold counterparts.
471 Figs. 5d and 5e also show that the relationship between resolved wave forcing and the QBO winds are
472 somewhat more complex. When zonal wind anomalies are close to zero, the coherent and modest
473 resolved westward wave forcing help the easterly shear zone of the QBO winds to propagate downwards
474 from the 10 hPa level to the 70 hPa level during both the cold and warm ENSO episodes while the



475 coherent and modest resolved eastward wave forcing help the westerly shear zone of the QBO winds to
476 propagate downwards only from the 20 hPa level to the 70 hPa level during both the cold and warm
477 ENSO episodes. At altitudes above the 20 hPa level, easterly jet cores are modestly weakened by the
478 resolved eastward wave forcing during the two extreme ENSO phases. In particular, Fig. 5f indicates
479 that at altitudes above the 30 hPa level the response of the resolved wave forcing to the ENSO acts to
480 slow down the downward propagation of the QBO during El Niño than during La Niña. However, the
481 parameterized gravity wave forcing shown in Fig. 5 clearly dominates over the resolved wave forcing,
482 which is consistent with the finding of DallaSanta et al. (2021) that the parameterized convective gravity
483 waves play a dominant role in generating the spontaneous QBO in the GISS E2.2 models.

484 Figs. 6a–6c depict the composite fields of the QBO winds (black contours) and TEM advection
485 averaged over all realizations of the Coupled–NINT–AP ensemble. Comparing Figs. 6a–6c with Fig. 5
486 reveals that the TEM advection composite is also larger than composite resolved wave forcing in the
487 Coupled–NINT–AP model. Thus, the QBO simulated by this model is mainly controlled by the gravity
488 wave forcing and the TEM advection. Figs. 6a–6b also show that the maximum positive and negative
489 advective tendencies are located above rather than below and propagate downward with the westerly and
490 easterly QBO jets, thus acting to slow down the downward propagation of the QBO, which is mainly
491 caused by the persistent tropical upwelling and a general feature of the QBO (Giorgetta et al. 2006; Rind
492 et al., 2014). Figs. 6c indicates that there exist stronger positive and negative advective tendencies above
493 the westerly and easterly QBO jets during El Niño than during La Niña. In other words, the TEM
494 advection alone leads to a slower phase speed of the QBO during El Niño than during La Niña. This is
495 not surprising because El Niño gives rise to a stronger tropical upwelling in the lower stratosphere (Calvo
496 et al., 2010; Simpson et al., 2011).



497 Figs. 6d–6f show the composite the QBO winds (black contours) and the composite sum of gravity
498 wave forcing, resolved wave forcing, and TEM advection averaged over all realizations of the Coupled–
499 NINT–AP ensemble. In other words, the upper, middle, and lower panels depict the sum of the fields
500 shown in all the corresponding panels of Figure 5 and Figs. 6a–6c. The pattern of the composite sum is
501 generally determined by the pattern of gravity wave forcing even though the latter is more coherent than
502 the former. Thus, we conclude that the shorter QBO period during El Niño simulated by Coupled–NINT–
503 AP is mainly caused by stronger gravity wave forcing during warm ENSO episodes. We also find that
504 stronger gravity wave forcing during warm ENSO events are simulated by AMIP–OMA–SP, AMIP–
505 OMA–AP, and Coupled–OMA–AP models (figures not shown), which help us understand why most
506 members from each of those four ensembles generate a spontaneous QBO whose phase speed is
507 statistically significantly greater during El Niño than during La Niña at the 5% significance level.

508 Now we explore how ENSO influences gravity wave forcing, resolved wave forcing, and TEM
509 advection simulated by the Coupled–NINT–SP model, i.e., the remaining model listed in Tables 1 and 2.
510 Contrasting between Fig. 7a and Fig. 5c reveals that the ensemble mean composite response to the ENSO
511 of gravity wave forcing simulated by Coupled–NINT–SP is substantially weaker than that simulated by
512 Coupled–NINT–AP. Although the Coupled–NINT–SP simulations still bring about enhanced westward
513 gravity wave forcing in the easterly shear zones of the simulated QBO winds during El Niño in contrast
514 to La Niña, the magnitude of the reinforcement is only about two thirds of that simulated by Coupled–
515 NINT–AP. In particular, in Fig. 7a there is no coherent pattern of enhanced eastward gravity wave
516 forcing in the westerly shear zones of the QBO winds simulated by Coupled–NINT–SP, which is in
517 glaring contrast to the coherent pattern of positive enhancement shown in Fig. 5c generated from the
518 Coupled–NINT–AP ensemble. Figs. 7b and 7c show that both resolved wave forcing and TEM advection
519 respond to the ENSO weakly and uniformly in the Coupled–NINT–SP ensemble simulations. Combining



520 all three composite fields together, Fig. 7d demonstrates that the ensemble mean of the Coupled–NINT–
521 SP simulations still simulates a coherent but much weaker response to the ENSO of resultant forcing at
522 altitudes above the 40 hPa level, which helps us to explain why only some of the Coupled–NINT–SP
523 ensemble runs can simulate a faster QBO descent rate during El Niño than during La Niña and the ENSO
524 does not make a difference in the phase speed of the QBO that is statistically significant at the 5%
525 significance level in any of those Coupled–NINT–SP runs.

526 **4.2 ENSO modulation of the generation and propagation of parameterized gravity waves**

527 A natural question that arises is how the simulated gravity wave forcing relates to the SST anomalies
528 of ENSO extremes specified in or simulated by the GISS E2.2 models listed in Table 1. Figs. 8a and 8b
529 show the ensemble averages of the composite SST anomalies averaged over all La Niña and El Niño
530 months respectively over the 1871–2013 period simulated by Coupled–NINT–AP. Comparing Figs. 8a
531 and 8b with Figs. 3a and 3b reveals that the amplitude of the ENSO simulated by Coupled–NINT–AP is
532 larger than the observed. Figs. 8a and 8b also indicate that the model has a capability to simulate the
533 ENSO amplitude asymmetry (Cane and Zebiak, 1987; Yu and Mechoso, 2001), namely, the amplitudes
534 of the ENSO are relatively larger during warm episodes than during cold episodes. As in Fig. 3 of Zhao
535 and Sun (2022), Figs. 8c depicts the sum of the composite SST anomalies shown in Figs. 8a and 8b that
536 they used to characterize the ENSO amplitude asymmetry. Their Fig. 3 reveals that most CMIP6 models
537 cannot simulate the pattern of a positive residual in the sum of the composites of ENSO extremes in the
538 tropical eastern Pacific. Further comparison between Fig. 3 in Zhao and Sun (2022) and Fig. 8c indicates
539 that the ENSO amplitude asymmetry simulated by Coupled–NINT–AP is only about 50% of that
540 simulated by the GISS-E2-1-H model discussed in their study whose ENSO amplitude asymmetry is
541 comparable to the observed. Since this study is chiefly concerned with the ENSO modulation of the



542 QBO period, we focus on the ensemble mean difference between the composite SST anomalies of ENSO
543 extremes, which can be interpreted as the peak-to-peak amplitude of the ENSO cycle.

544 Comparing Fig. 9a with Fig. 3c indicates that the peak-to-peak ENSO amplitude derived from the
545 HadISST1 dataset over the 1871–2013 period is somewhat smaller than that derived from the ERSSTv5
546 dataset over the 1953–2015 period, which is consistent with the finding by Grothe et al. (2019) that the
547 increase in the ENSO variability is statistically significant (>95% confidence) from the preindustrial to
548 recent era, no matter whether the latter is defined by the previous 30, 50, 75, or 100 years before 2016.
549 Fig. 8c and Fig. 9 also reveal that the ENSO amplitude simulated by Coupled–OMA–AP is somewhat
550 stronger than that simulated by Coupled–NINT–AP which in turn is substantially greater than that
551 simulated by Coupled–NINT–SP. Even though the ENSO amplitude from Coupled–NINT–SP is
552 weakest among three coupled models, it is noticeably greater than that specified in the AMIP–OMA–SP
553 and AMIP–OMA–AP models.

554 We also ascertain that the Hadley circulation simulated by each of the five models listed in Table 1
555 strengthens and weakens during warm and cold ENSO episodes respectively, which is consistent with
556 the finding by Oort and Yienger (1996); that the responses of the Hadley circulation to ENSO extremes
557 are comparable between the Coupled–OMA–AP and Coupled–NINT–AP ensembles; that both of them
558 are substantially stronger than that simulated by Coupled–NINT–SP, which is stronger than the
559 simulated responses from two AMIP models whose responses to ENSO extremes are comparable
560 (figures not shown).

561 Schirber (2015) discovered that the parameterized gravity wave mean momentum source is about 15%
562 larger in the El Niño ensemble than in the La Niña ensemble because the El Niño leads to enhanced
563 precipitation and convective heating. Similarly, we calculate the absolute value of convective
564 momentum fluxes (ACMF) at the source altitude and composite the ACMF anomalies averaged over the



565 latitudinal belt between 5°S and 5°N from El Niño and La Niña categories respectively over the 1871–
566 2013 period. Fig. 10 shows the composite difference in the equatorial mean ACMF anomalies between
567 El Niño and La Niña over the 1871–2013 period, indicating that the absolute momentum fluxes at the
568 source levels over the equatorial belt is larger during El Niño episodes than during La Niña episodes for
569 each of 24 runs listed in Table 1. This finding is consistent with that of Geller et al. (2016b), Alexander
570 et al. (2017), and Kang et al. (2018). The ensemble mean difference in the absolute momentum fluxes at
571 the source levels averaged over that equatorial belt between El Niño and La Niña is obtained as 0.07,
572 0.15, 0.10, 0.12, 0.12 mPa for AMIP–OMA–SP, AMIP–OMA–AP, Coupled–NINT–SP, Coupled–
573 NINT–AP, and Coupled–OMA–AP, respectively. Note that these composite differences in ACMF
574 between El Niño and La Niña translate into ACMF being about 10–20% larger in the El Niño ensembles
575 than in the La Niña ensembles, thus agree with the Schirber (2015). Since the QBO period is inversely
576 dependent upon the momentum flux (Plumb, 1977), the differences in equatorial absolute momentum
577 fluxes at the source altitude contribute to shortening and lengthening of the simulated QBO period during
578 warm and cold ENSO phases, respectively.

579 Fig. 3 shows that the locations of warmest SSTs shift from the maritime continent during La Niña
580 episodes to the central and eastern equatorial Pacific during El Niño episodes. Since strong convective
581 activities over tropical oceans are generally located above the regions where the SSTs exceed 26°–28° C
582 (Graham and Barnett, 1987; Zhang, 1993), strong convective activities also shift eastward from cold to
583 warm ENSO phases, as illustrated in Fig.2. Using satellite data, the climatological study by Sullivan et
584 al. (2019) demonstrated that the occurrence of organized deep convection during El Niño events
585 increases threefold in the central and eastern Pacific and decreases twofold outside of these regions in
586 contrast to that during La Niña events. It is well-established that the Walker circulation strengthens
587 during La Niña and weakens during El Niño (Bjerknes, 1969).



588 To illustrate how the ENSO influences the Walker circulation, we first obtain the ERA5 (Hersbach
589 et al., 2020) monthly mean zonal winds over the 1979–2015 period from the European Centre for
590 Medium-Range Weather Forecasts (ECMWF), Copernicus Climate Change Service (C3S). Next, we
591 construct the equatorial zonal winds as the zonal winds averaged from 5°S to 5°N. Then we define the
592 equatorial winds during La Niña and El Niño as the equatorial winds averaged over all months that fall
593 into the La Niña and El Niño categories, respectively. Fig. 11 illuminates that the Walker circulation
594 during El Niño is substantially weaker than that during La Niña over the equatorial Pacific and the eastern
595 equatorial Indian ocean. In particular, the westerlies above the central and eastern Pacific and the
596 easterlies above the maritime continent and the eastern Indian ocean are substantially weaker in the upper
597 equatorial troposphere during in El Niño than during La Niña. Kawatani et al. (2019) argue that the
598 weaker upper tropospheric winds during El Niño episodes enable a greater amount of gravity wave
599 momentum fluxes to be transferred from the troposphere into stratosphere because less gravity waves
600 are filtered out. This argument assumes critical-level absorption of otherwise weakly damped, vertically
601 propagating gravity waves, which was adopted by Lindzen and Holton (1968). The weaker Walker
602 circulation leads to a shorter QBO period during El Niño while the stronger Walker circulation results
603 in a longer QBO period during La Niña.

604 To illuminate how the E2.2 models simulate the response of upper tropospheric winds to the ENSO
605 extremes, we first construct the anomalous monthly zonal winds based on centered 30-year base periods
606 updated every 5 years as per section 2 or section 3, which ensures a proper extraction of the ENSO signal
607 by removing the secular and multi-decadal variations in zonal winds. Next, we average the anomalies of
608 zonal winds from 5°S to 5°N to obtain the monthly equatorial zonal winds anomalies between 1871 and
609 2013. Then we composite the equatorial zonal wind anomalies during La Niña and El Niño by averaging
610 them over all months that fall into the La Niña and El Niño categories, respectively. Fig. 12 depicts the



611 ensemble mean composite difference in the equatorial zonal wind anomalies between warm and cold
612 ENSO extremes simulated by the E2.2 models listed in Table 1. The patterns of the simulated wind
613 anomalies shown in Fig. 12 are very similar to that derived from the ERA5 reanalysis shown in Fig. 11c.
614 Namely, the weakened Walker circulation simulated by the E2.2 models during El Niño episodes results
615 in weaker upper tropospheric westerlies over the central and eastern equatorial Pacific and weaker upper
616 tropospheric easterlies over the maritime continent and eastern equatorial Indian ocean while the
617 intensified Walker circulation simulated by the E2.2 models during La Niña episodes leads to stronger
618 upper tropospheric westerlies over the central and eastern equatorial Pacific and stronger upper
619 tropospheric easterlies over the maritime continent and eastern equatorial Indian ocean. The difference
620 in the wind filtering of upward propagating gravity waves causes a greater transfer of gravity wave
621 momentum fluxes into the tropical stratosphere during El Niño episodes than during La Niña episodes,
622 leading to a shorter QBO period during El Niño events than during La Niña events. Further comparison
623 between Figs. 11 and 12 reveal that the contrast in the Walker circulation between warm and cold ENSO
624 extremes simulated by two AMIP models, i.e., AMIP–OMA–SP and AMIP–OMA–AP, is comparable
625 to that derived from the ERA5 reanalysis. However, the difference in the Walker circulation over the
626 central and eastern equatorial Pacific between warm and cold ENSO extremes simulated by three
627 coupled ocean-atmosphere models, i.e., Coupled–NINT–SP, Coupled–NINT–AP, and Coupled–OMA–
628 AP, is substantially smaller than that derived from the ERA5 reanalysis.

629 While the comparison of the observed and simulated changes in the Walker circulation between warm
630 and cold ENSO extremes shown in Figs. 11 and 12 can account for a shorter QBO period simulated by
631 all GISS E2.2 models and can also explain why the two AMIP models can better capture the ENSO
632 modulation of the QBO period than the Coupled–NINT–SP model as indicated in Table 2, it nether can
633 explain why both the Coupled–NINT–AP and Coupled–OMA–AP models can comparably capture the



634 ENSO modulation of the QBO period as two AMIP models nor can illuminate why these two coupled
635 models with the altered physics perform better than the coupled model with the standard physics (i.e.,
636 Coupled–NINT–SP). However, further comparing the simulated SST changes between warm and cold
637 ENSO extremes shown in Figs. 8 and 9 hints that the unduly amplified ENSO in the coupled AP runs
638 holds the key to those unsettled issues that is detailed as follows.

639 Using a large ensemble of multiple climate models, Serva et al. (2020) discovered that the AMIP
640 historical runs generally better capture the ENSO modulation of the QBO period than the coupled ocean-
641 atmosphere historical simulations. In particular, among a few coupled ocean-atmosphere models that do,
642 to various extents, capture the ENSO modulation of the QBO period, the common feature is that each of
643 them can largely simulate the observed OLR anomaly pattern shown in Fig. 2c albeit the magnitudes of
644 those simulated OLR anomalies from their historical runs are roughly 50% stronger than the observed
645 (for more details, refer to their Fig. 8 in Serva et al., 2020). For the sake of comparison, we construct the
646 ensemble mean composite difference in the OLR anomalies between warm and cold ENSO extremes in
647 the same way we constructed the ensemble mean composite difference in the zonal wind anomalies
648 depicted in Fig. 12.

649 Figs. 13a and 13b show that the patterns of the OLR anomalies simulated by AMIP–OMA–SP and
650 AMIP–OMA–AP largely resemble the observed one shown in Fig. 2c. Although the pattern simulated
651 by AMIP–OMA–AP matches better with the observed, the convective activities during El Niño episodes
652 simulated by AMIP–OMA–SP and AMIP–OMA–AP are apparently inadequate over the region where
653 the upper tropospheric westerlies weaken most conspicuous during warm ENSO extremes shown in Figs.
654 12a and 12b, respectively. Thus, although the contrast in the wind filtering of gravity waves between El
655 Niño and La Niña episodes simulated by the two AMIP E2.2 models are comparable to the observed,
656 the difference in the gravity wave momentum flux transferred into the equatorial stratosphere between



657 warm and cold ENSO extremes should be smaller than the observed. This partly explains why the
658 observed contrast between the mean QBO period during El Niño episodes (i.e., 25.1 months) and the
659 mean QBO period during La Niña episodes (i.e., 34.5 months) is higher than that simulated by the two
660 AMIP models shown in Table 2 (i.e., E1 and E2 in Table 2). As exhibited by the coupled models capable
661 of simulating the ENSO modulation of the QBO period, Figs. 13d and 13e show that the contrast in the
662 OLR anomalies between warm and cold ENSO extremes simulated by Coupled–NINT–AP and
663 Coupled–OMA–AP are apparently sharper than the observed one shown in Fig. 2c. In particular, the
664 tropical convection in the central and eastern Pacific during El Niño episodes simulated by Coupled–
665 NINT–AP and Coupled–OMA–AP is both more extensive and more intensive than that simulated by the
666 two AMIP models shown in Figs. 13a and 13b, which is consistent with the fact that the composite
667 differences in the SST anomalies simulated by Coupled–NINT–AP shown in Fig. 8d and by Coupled–
668 OMA–AP shown in Fig. 9c are substantially sharper than that prescribed in the two AMIP models shown
669 in Fig. 9a. Thus, even though the wind filtering of gravity waves during El Niño episodes simulated by
670 Coupled–NINT–AP and Coupled–OMA–AP shown in Figs 12d and 12e are significantly smaller than
671 that simulated by AMIP–OMA–SP and AMIP–OMA–AP shown in Figs 12a and 12b, respectively, the
672 combined effect of the lower contrast in the wind filtering and the higher contrast in the amount of
673 gravity wave momentum fluxes generated by convective activities between warm and cold ENSO
674 extremes over the central and eastern tropical Pacific results in a comparable ENSO modulation of the
675 QBO period simulated by AMIP–OMA–SP and AMIP–OMA–AP to that simulated by the two AMIP
676 models as illustrated in Table 2. Finally, comparing Fig. 13c with Fig. 2c and other four panels in Fig.
677 13 reveals that convective activities during the warm ENSO phase simulated by the Coupled–NINT–SP
678 model are substantially weaker than both the observed and those simulated by other four models list in
679 Table 1. Combining the small composite OLR difference shown in Fig. 13c and the small difference in



680 the wind filtering shown in Fig. 9c between warm and cold ENSO extremes over the central and eastern
681 equatorial Pacific results in a low contrast in gravity wave forcing between warm and cold ENSO phases
682 shown in Fig. 7a, which, short of the compensating effect of the excessively amplified ENSO in
683 Coupled–NINT–AP and Coupled–OMA–AP simulations, leads to a relatively weaker ENSO modulation
684 of the QBO period simulated by the Coupled–NINT–SP model as illustrated in Table 2.

685

686 **5. Discussion and Conclusions**

687 Both Kawatani et al. (2019) and Serva et al. (2020) pointed out that a relatively high horizontal
688 resolution is necessary to simulate the ENSO modulation of the QBO period. Employing an earth system
689 model with T42 ($\sim 2.79^\circ$) horizontal resolution, Kawatani et al. (2019) further demonstrated that the
690 ENSO modulation of the QBO could not be simulated with their fixed gravity wave sources. Serva et al.
691 (2020) also pointed out that the reliance on stationary parameterizations of gravity waves is partly
692 responsible for failing to simulate the observed modulation of the QBO by the ENSO in current climate
693 models.

694 Rind et al. (1988) implemented various interactive gravity wave sources in the GISS climate models.
695 With the momentum flux of the parameterized convective waves dependent on the convective mass flux,
696 buoyancy frequency at the top of the convective region, wind velocity averaged over the convective
697 layers, etc. and with a horizontal resolution of 2° latitude by 2.5° longitude, all the five versions of GISS
698 E2.2 models in this study can simulate the ENSO modulation of the QBO period to various degrees. For
699 each of 24 runs conducted in this study, the absolute momentum fluxes at the source levels over the
700 equatorial belt is larger during El Niño episodes than during La Niña episodes, leading to a shorter and
701 longer QBO period, respectively.



702 Realistic simulation of the ENSO modulation of the QBO periods entails the realistic simulation of
703 both the ENSO and the QBO. With the realistic SSTs specified, both the composite difference in the
704 Walker circulation and the composite OLR difference between warm and cold ENSO extremes simulated
705 by the two AMIP E2.2 models are close to the observed. Since the AMIP model with the “altered physics”
706 performs better than that with the “standard physics” as far as the simulated OLR is concerned, the
707 ensemble mean difference in the QBO period between La Niña and El Niño episodes (i.e., ~4.5 months)
708 simulated by AMIP–OMA–AP is larger than that simulated by AMIP–OMA–SP (i.e., ~3.9 months),
709 which indicates that convective parameterization scheme is important not only for simulating the
710 resolved waves as pointed out by Horinouchi et al. (2003) and Lott et al. (2014), but also for
711 parameterizing gravity waves. However, the convective activities simulated by both AMIP E2.2 models
712 are still inadequate over the central and eastern equatorial Pacific as compared to the observed, which
713 may partly account for why the ensemble mean differences in the QBO period between La Niña and El
714 Niño episodes simulated by both AMIP models are smaller than the observed difference (i.e., ~9.4
715 months).

716 Although the simulated Walker circulations associated with the ENSO cycle are comparable among
717 the three coupled ocean-atmosphere models in this study, the E2.2 model with the “standard physics”
718 performs well in its simulated SSTs which is very close to the observed while the ENSO amplitudes
719 simulated by other two models with the “altered physics” are substantially greater than observed. The
720 model with the “standard physics” not only fails to properly simulate the shift of the strongest convection
721 from the maritime continent during La Niña to the central and eastern equatorial Pacific during El Niño,
722 but also grossly fail to simulate the sufficient amplitude of the OLR concomitant with the ENSO cycle.
723 The weaker response of the Walker circulation and convective activities to the ENSO cycle together
724 with the dislocated centers of convection concomitant to cold and warm ENSO extremes leads to the



725 smallest ensemble mean difference in the QBO period between La Niña and El Niño episodes (i.e., ~2.7
726 months) simulated by the Coupled–NINT–SP model. The weaker variation of the Walker circulation and
727 the excessive change in convection compensate to give an impression of realistically simulating the
728 ENSO modulation of the QBO period by the other two models with the “altered physics”, i.e., Coupled–
729 NINT–AP and Coupled–OMA–AP, with their ensemble mean differences in the QBO period between
730 La Niña and El Niño episodes being ~4.8 and ~5.6 months, respectively. However, it is worth pointing
731 out that we don’t regard those two models as the best among the five models listed in Table 1 because
732 the relatively satisfactory results are achieved in a compensatory, thus unrealistic, way. Serva et al. (2020)
733 conducted both the atmosphere-only and coupled historical simulations and found that the peak-to-peak
734 amplitudes of the OLR associated with the ENSO cycle are two times larger than the observed for a few
735 models that relatively well capture the ENSO modulation of the QBO period, which together with our
736 results suggests that the parameterized convection is a linchpin of realistically simulating the ENSO, the
737 QBO, and the ENSO modulation of the QBO.

738 Intriguingly, the simulated difference in the QBO period between La Niña and El Niño is 6.2 months
739 from the first realization simulated by Coupled–NINT–SP. However, it is not statistically significant at
740 the 5% significance level. Meanwhile, the differences in the QBO period between La Niña and El Niño
741 from most of the realizations simulated by Coupled–NINT–AP and Coupled–OMA–AP are apparently
742 less than 6.2 months but are all statistically significant. To gain a deeper insight, we calculate the
743 frequency power spectra of standardized ONIs derived from the observed and simulated SSTs. Fig. 14a
744 depicts the power spectral densities (PSD) of standardized ONI between 1953 and 2015 derived from
745 the NOAA ERSSTv5 SST while Fig. 14b delineates the PSD of standardized ONI between 1871 and
746 2013 derived from the HadISST1 dataset. Figs. 14a and 14b show that although the ENSO accounts for
747 the lion’s share of SST variabilities, there is a good amount of SST variabilities on the decadal and



748 multidecadal time scales. Fig. 14d illustrates the PSD of standardized ONI between 1871 and 2013
749 simulated by the second realization of Coupled–NINT–AP while Fig. 14e illuminates that simulated by
750 the second realization of Coupled–OMA–AP, which demonstrate that the ENSO overwhelmingly
751 dominates over any other noises in SST variabilities simulated by those E2.2 models with the “altered
752 physics”. Furthermore, Fig. 14c shows the PSD of standardized ONI between 1871 and 2013 simulated
753 by the first realization of Coupled–NINT–SP. Apparently, the SST variabilities simulated by the E2.2
754 model with the “standard physics” are comparable to the observed, thus more realistic. The smaller ratio
755 of the ENSO signal to the noise simulated by the first realization of Coupled–NINT–SP and the much
756 larger ratio simulated by the second realizations of the E2.2 models with “alter physics” explain why the
757 difference of 6.2 months in the QBO period between La Niña and El Niño from the former is not
758 statistically significant while why the differences of 2.6 and 4.8 months from the latter are statistically
759 significant as shown in Table 2.

760 None of the E2.2 configurations robustly simulate an ENSO modulation of QBO amplitude,
761 consistent with the weaker signal present in observations (Yuan et al., 2014). In order to realistically
762 simulate the ENSO modulation of the QBO, various aspects of climate models such as the SSTs, the
763 Walker circulations, the parameterizations of convection and gravity waves need to be further improved,
764 which is fortunately ongoing under the auspices of the SPARC Quasi-Biennial Oscillation initiative
765 (Butchart et al., 2018).

766

767 **Data availability**

768 The monthly mean zonal winds from Free University of Berlin are obtained from [https://www.geo.fu-](https://www.geo.fu-berlin.de/en/met/ag/strat/produkte/qbo/index.html)
769 [berlin.de/en/met/ag/strat/produkte/qbo/index.html](https://www.geo.fu-berlin.de/en/met/ag/strat/produkte/qbo/index.html). The NOAA ERSSTv5 SST is acquired from
770 <https://www.ncei.noaa.gov/products/extended-reconstructed-sst>. The NCEI OLR is downloaded from



771 <https://www.ncei.noaa.gov/products/climate-data-records/outgoing-longwave-radiation-monthly>. The
772 ERA5 monthly mean zonal winds are obtained from the ECMWF C3S at Climate Data Store:
773 <https://cds.climate.copernicus.eu/>. The GISS ModelE E2.2 data are available from the Earth System Grid
774 Federation and also from the NASA Center for Climate Simulation data portal (including non-CMIP6
775 simulations).

776

777 **Author contributions**

778 All authors made equal contributions to this work.

779

780 **Competing interests**

781 The authors declare that they have no conflict of interest.

782

783 **Acknowledgements:** Climate modeling at GISS is supported by the NASA Modeling, Analysis and
784 Prediction program, and resources supporting this work were provided by the NASA High-End
785 Computing (HEC) Program through the NASA Center for Climate Simulation (NCCS) at Goddard Space
786 Flight Center.

787

788 **References**

789 Alexander, M. J., Ortland, D. A., Grimsdell, A. W., and Kim, J.-E.: Sensitivity of Gravity Wave Fluxes
790 to Interannual Variations in Tropical Convection and Zonal Wind, *J. Atmos. Sci.*, 74, 2701–
791 2716, <https://doi.org/10.1175/JAS-D-17-0044.1>, 2017.



- 792 Andrews, D. G., Mahlman, J. D., and Sinclair, R. W.: Eliassen–Palm diagnostics of wave-mean flow
793 interaction in the GFDL” SKYHI” general circulation model, *J. Atmos. Sci.*, 40, 2768–2784,
794 [https://doi.org/10.1175/1520-0469\(1983\)040%3C2768:ETWATM%3E2.0.CO;2](https://doi.org/10.1175/1520-0469(1983)040%3C2768:ETWATM%3E2.0.CO;2), 1983.
- 795 Andrews, D. G., Holton, J. R., and Leovy, C. B.: *Middle Atmosphere Dynamics*, Academic Press, 489
796 pp, 1987.
- 797 Angell, J. K.: On the variation in period and amplitude of the quasi-biennial oscillation in the equatorial
798 stratosphere, 1951–85, *Mon. Weather Rev.*, 114, 2272–2278, [https://doi.org/10.1175/1520-0493\(1986\)114%3C2272:OTVIPA%3E2.0.CO;2](https://doi.org/10.1175/1520-0493(1986)114%3C2272:OTVIPA%3E2.0.CO;2), 1986.
- 800 Anstey, J. A., Banyard, T. P., Butchart, N., Coy, L., Newman, P. A., Osprey, S., and Wright, C. J.:
801 Prospect of Increased Disruption to the QBO in a Changing Climate, *Geophys. Res. Lett.*, 48,
802 e2021GL093058, <https://doi.org/10.1029/2021GL093058>, 2021.
- 803 Baldwin, M. P., Gray, L. J., Dunkerton, T. J., Hamilton, K., Haynes, P. H., Randel, W. J., Holton, J. R.,
804 Alexander, M. J., Hirota, I., Horinouchi, T., Jones, D. B. A., Kinniersley, J. S., Marquardt, C., Sato,
805 K., and Takahashi, M.: The Quasi-biennial oscillation, *Rev. Geophys.*, 39, 179–229,
806 <https://doi.org/10.1029/1999RG000073>, 2001.
- 807 Bauer, S. E., Tsigaridis, K., Faluvegi, G., Kelley, M., Lo, K. K., Miller, R. L., Nazarenko, L., Schmidt,
808 G. A., and Wu, J.: Historical (1850–2014) Aerosol Evolution and Role on Climate Forcing Using
809 the GISS ModelE2.1 Contribution to CMIP6, *J. Adv. Model. Earth Sy.*, 12, e2019MS001978,
810 <https://doi.org/10.1029/2019ms001978>, 2020.
- 811 Bergman, J. W. and Salby, M. L.: Equatorial wave activity derived from fluctuations in observed
812 convection, *J. Atmos. Sci.* 51, 3791–3806, [https://doi.org/10.1175/1520-0469\(1994\)051%3C3791:EWADFF%3E2.0.CO;2](https://doi.org/10.1175/1520-0469(1994)051%3C3791:EWADFF%3E2.0.CO;2), 1994.



- 814 Bjercknes, J.: Atmospheric teleconnections from the equatorial Pacific, *Mon. Weather Rev.*, 97, 163–172,
815 [https://doi.org/10.1175/1520-0493\(1969\)097%3C0163:ATFTEP%3E2.3.CO;2](https://doi.org/10.1175/1520-0493(1969)097%3C0163:ATFTEP%3E2.3.CO;2), 1969.
- 816 Bushell, A. C., Anstey, J. A., Butchart, N., Kawatani, Y., Osprey, S. M., Richter, J. H., Serva, F.,
817 Braesicke, P., Cagnazzo, C., Chen, C.-C., Chun, H.-Y., Garcia, R. R., Gray, L. J., Hamilton, K.,
818 Kerzenmacher, T., Kim, Y.-H., Lott, F., McLandress, C., Naoe, H., Scinocca, J., Smith, A. K.,
819 Stockdale, T. N., Versick, S., Watanabe, S., Yoshida, K., and Yukimoto, S.: Evaluation of the Quasi-
820 Biennial Oscillation in global climate models for the SPARC QBO-initiative, *Q. J. Roy. Meteor.*
821 *Soc.*, 1–31, <https://doi.org/10.1002/qj.3765>, 2020.
- 822 Butchart, N., Anstey, J., Hamilton, K., Osprey, S., McLandress, C., Bushell, A. C., Kawatani, Y., Kim,
823 Y.-H., Lott, F., Scinocca, J., Stockdale, T.N., Andrews, M., Bellprat, O., Braesicke, P., Cagnazzo,
824 C., Chen, C.-C., Chun, H.-Y., Dobrynin, M., Garcia, R., Garcia-Serrano, J., Gray, L.J., Holt, L.,
825 Kerzenmacher, T., Naoe, H., Pohlmann, H., Richter, J. H., Scaife, A.A., Schenzinger, V., Serva, F.,
826 Versick, S., Watanabe, S., Yoshida, K. and Yukimoto, S.: Overview of experiment design and
827 comparison of models participating in phase 1 of the SPARC Quasi-Biennial Oscillation initiative
828 (QBOi), *Geoscientific Model Development*, 11, 1009–1032. [https://doi.org/10.5194/gmd-11-1009-](https://doi.org/10.5194/gmd-11-1009-2018)
829 [2018](https://doi.org/10.5194/gmd-11-1009-2018), 2018.
- 830 Calvo, N., Garcia, R. R., Randel, W. J., and Marsh, D. R.: Dynamical mechanism for the increase in
831 tropical upwelling in the lowermost tropical stratosphere during warm ENSO events, *J. Atmos. Sci.*,
832 67, 2331–2340, <https://doi.org/10.1175/2010JAS3433.1>, 2010.
- 833 Cane, M. and Zebiak, S. E.: Prediction of El Niño events using a physical model, in *Atmospheric and*
834 *Oceanic Variability*, edited by H. Cattle, Royal Meteorological Society Press, London, 153-182,
835 1987.



- 836 Christiansen, B., Yang, S., and Madsen, M. S.: Do strong warm ENSO events control the phase of the
837 stratospheric QBO?, *Geophys. Res. Lett.*, 43, 10489–10495,
838 <https://doi.org/10.1002/2016GL070751>, 2016.
- 839 Collimore, C. C., Martin, D. W., Hitchman, M. H., Huesmann, A., and Waliser, D. E.: On the
840 relationship between the QBO and tropical deep convection, *J. Climate*, 16, 2552–2568,
841 [https://doi.org/10.1175/1520-0442\(2003\)016%3C2552:OTRBTQ%3E2.0.CO;2](https://doi.org/10.1175/1520-0442(2003)016%3C2552:OTRBTQ%3E2.0.CO;2), 2003.
- 842 DallaSanta, K., Orbe, C., Rind, D., Nazarenko, L., and Jonas, J.: Dynamical and trace gas responses of
843 the Quasi-Biennial Oscillation to increased CO₂, *J. Geophys. Res. Atmos.*, 126, e2020JD034151.
844 <https://doi.org/10.1029/2020JD034151>, 2021.
- 845 Domeisen, D. I. V., Garfinkel, C. I., and Butler, A. H.: The Teleconnection of El Niño Southern
846 Oscillation to the Stratosphere, *Rev. Geophys.*, 57, 5–
847 47, <https://doi.org/10.1029/2018RG000596>, 2019.
- 848 Garfinkel, C. I. and Hartmann, D. L.: Effects of El Niño – South- ern Oscillation and the Quasi-Biennial
849 Oscillation on polar tem- peratures in the stratosphere, *J. Geophys. Res.*, 112, D19112,
850 <https://doi.org/10.1029/2007JD008481>, 2007.
- 851 Garfinkel, C. I. and Hartmann, D. L.: The influence of the quasi-biennial oscillation on the troposphere
852 in winter in a hierarchy of models. Part I: Simplified dry GCMs, *J. Atmos. Sci.*, 68, 1273–1289,
853 <https://doi.org/10.1175%2F2011JAS3665.1>, 2011a.
- 854 Garfinkel, C. I. and Hartmann, D. L.: The influence of the quasi-biennial oscillation on the troposphere
855 in winter in a hierarchy of models. Part II: Perpetual winter WACCM runs, *J. Atmos. Sci.*, 68, 2026–
856 2041, <https://doi.org/10.1175%2F2011JAS3702.1>, 2011b.
- 857 Geller, M. A., Zhou, T., Shindell, D., Ruedy, R., Aleinov, I., Nazarenko, L., Tausnev, N. L., Kelley, M.,
858 Sun, S., Cheng, Y., Field, R. D., and Faluvegi, G.: Modeling the QBO-improvements resulting from



- 859 higher-model vertical resolution, *J. Adv. Model. Earth Syst.*, 8, 1092–1105,
860 <https://doi.org/10.1002/2016MS000699>, 2016a.
- 861 Geller, M. A., Zhou, T., and Yuan, W.: The QBO, gravity waves forced by tropical convection, and
862 ENSO, *J. Geophys. Res. Atmos.*, 121, 8886–8895, <https://doi.org/10.1002/2015JD024125>, 2016b.
- 863 Giorgetta, M. A., Bengtson, L., and Arpe, K.: An investigation of QBO signals in the east Asian and
864 Indian monsoon in GCM experiments, *Climate Dynamics*, 15, 435–450,
865 <https://doi.org/10.1007/s003820050292>, 1999.
- 866 Giorgetta, M. A., Manzini, E., and Roeckner, E., Esch, M., and Bengtsson, L.: Climatology and forcing
867 of the quasi-biennial oscillation in the MAECHM5 model, *J. Climate*, 19, 3882–3901,
868 <https://doi.org/10.1175/JCLI3830.1>, 2006.
- 869 Graham, N. E. and Barnett, T. P.: Sea surface temperature, surface wind divergence, and convection over
870 tropical oceans, *Science*, 238, 657–659, <https://doi.org/10.1126/science.238.4827.657>, 1987.
- 871 Gray, W. M.: Atlantic seasonal hurricane frequency. Part I: El Niño and 30-mb quasi-biennial oscillation
872 influences, *Mon. Wea. Rev.*, 112, 1649–1688, [https://doi.org/10.1175/1520-0493\(1984\)112%3C1649:ASHFPI%3E2.0.CO;2](https://doi.org/10.1175/1520-0493(1984)112%3C1649:ASHFPI%3E2.0.CO;2), 1984.
- 874 Gray, W. M., Sheaffer, J. D., and Knaff, J.: Influence of the stratospheric QBO on ENSO variability, *J.*
875 *Meteor. Soc. Jpn.*, 70, 975–995, https://doi.org/10.2151/jmsj1965.70.5_975, 1992.
- 876 Grothe, P. R., Cobb, K. M., Liguori, G., Di Lorenzo, E., Capotondi, A., Lu, Y., Cheng, H., Edwards, R.L.,
877 Southon, J. R., Santos, G. M., Deocampo, D. M., Lynch-Stieglitz, J., Chen, T., Sayani, H. R.,
878 Thompson, D. M., Conroy, J. L., Moore, A. L., Townsend, K., Hagos, M., O'Connor, G., and Toth,
879 L. T.: Enhanced El Niño–Southern oscillation variability in recent decades, *Geophys. Res. Lett.*, 47,
880 e2019GL083906, <https://doi.org/10.1029/2019GL083906>, 2019.



- 881 Hamilton, K., Osprey, S., and Butchart, N.: Modeling the stratosphere’s “heartbeat,” *Eos*, 96, p. 8,
882 <https://doi.org/10.1029/2015EO032301>, 2015.
- 883 Hansen, F., Matthes, K., and Wahl, S.: Tropospheric QBO–ENSO interactions and differences between
884 the Atlantic and Pacific, *J. Climate*, 29, 1353–1368, <https://doi.org/10.1175/JCLI-D-15-0164.1>,
885 2016
- 886 Hasebe, F.: Quasi-biennial oscillations of ozone and diabatic circulation in the equatorial stratosphere, *J.*
887 *Atmos. Sci.*, 51, 729–745, [https://doi.org/10.1175/1520-
888 0469\(1994\)051%3c0729:QBOOOA%3e2.0.CO;2](https://doi.org/10.1175/1520-0469(1994)051%3c0729:QBOOOA%3e2.0.CO;2), 1994.
- 889 Hersbach, H., Bell, B., Berrisford, P., Hirahara, S., Horányi, A., Muñoz-Sabater, J., Nicolas, J., Peubey,
890 C., Radu, R., Schepers, D., Simmons, A., Soci, C., Abdalla, S., Abellan, X., Balsamo, G., Bechtold,
891 P., Biavati, G., Bidlot, J., Bonavita, M., Chiara, G., Dahlgren, P., Dee, D., Diamantakis, M., Dragani,
892 R., Flemming, J., Forbes, R., Fuentes, M., Geer, A., Haimberger, L., Healy, S., Hogan, R. J., Hólm,
893 E., Janisková, M., Keeley, S., Laloyaux, P., Lopez, P., Lupu, C., Radnoti, G., Rosnay, P., Rozum, I.,
894 Vamborg, F., Villaume, S., and Thépaut, J.-N.: The ERA5 global reanalysis, *Q. J. Roy. Meteor. Soc.*,
895 online first, <https://doi.org/10.1002/qj.3803>, 2020.
- 896 Hitchman, M. H., and Huesmann, A. S.: Seasonal influence of the quasi-biennial oscillation on
897 stratospheric jets and Rossby wave breaking, *J. Atmos. Sci.*, 66, 935–946,
898 <https://doi.org/10.1175%2F2008JAS2631.1>, 2009.
- 899 Ho, C.-H., Kim, H.-S., Jeong, J.-H., and Son, S.-W.: Influence of stratospheric quasi-biennial oscillation
900 on tropical cyclone tracks in the western North Pacific, *Geophys. Res. Lett.*, 36, L06702,
901 <http://dx.doi.org/10.1029/2009GL037163>, 2009.
- 902 Holton, J.: Waves in the equatorial stratospheric generated by tropospheric heat resources, *J. Atmos. Sci.*,
903 27, 368–375, [https://doi.org/10.1175/1520-0469\(1972\)029%3C0368:WITESG%3E2.0.CO;2](https://doi.org/10.1175/1520-0469(1972)029%3C0368:WITESG%3E2.0.CO;2), 1972.



- 904 Holton, J. R. and Lindzen, R. S.: An updated theory for the quasi-biennial cycle of the tropical
905 stratosphere, *J. Atmos. Sci.*, 29, 1076–1080, [https://doi.org/10.1175/1520-0469\(1972\)029%3c1076:AUTFTQ%3e2.0.CO;2](https://doi.org/10.1175/1520-0469(1972)029%3c1076:AUTFTQ%3e2.0.CO;2), 1972.
- 907 Holton, J. R. and Tan, H.: The Influence of the equatorial quasi-biennial oscillation on the global
908 circulation at 50 mb, *J. Atmos. Sci.*, 37, 2200–2208, [https://doi.org/10.1175/1520-0469\(1980\)037%3c2200:TIOTEQ%3e2.0.CO;2](https://doi.org/10.1175/1520-0469(1980)037%3c2200:TIOTEQ%3e2.0.CO;2), 1980.
- 910 Horinouchi, T., Pawson, S., Shibata, K., Manzini, E., Giorgetta, M., and Sassi, F.: Tropical cumulus
911 convection and upward propagating waves in middle-atmospheric GCMs, *J. Atmos. Sci.*, 60, 2765–
912 2782, [https://doi.org/10.1175/1520-0469\(2003\)060%3C2765:TCCA UW%3E2.0.CO;2](https://doi.org/10.1175/1520-0469(2003)060%3C2765:TCCA UW%3E2.0.CO;2), 2003.
- 913 Huang, B. H., Hu, Z. Z., Kinter, J. L., Wu, Z. H., and Kumar, A.: Connection of stratospheric QBO with
914 global atmospheric general circulation and tropical SST. Part I: Methodology and composite life
915 cycle, *Climate Dynamics*, 38, 1–23, <https://doi.org/10.1007%2Fs00382-011-1250-7>, 2012.
- 916 Huang, B., Thorne, P. W., Banzon, V. F., Boyer, T., Chepurin, G., Lawrimore, J. H., Menne M. J., Smith,
917 T. M., Vose R. S., and Zhang, H. M.: Extended reconstructed sea surface temperature, version 5
918 (ERSSTv5): upgrades, validations, and intercomparisons, *J. Climate*, 30, 8179–
919 8205, <https://doi.org/10.1175/JCLI-D-16-0836.1>, 2017.
- 920 Kang, M.-J., Chun, H.-Y., Kim, Y.-H., Preusse, P., and Ern, M.: Momentum flux of convective gravity
921 waves derived from an offline gravity wave parameterization. Part II: Impacts on the Quasi-Biennial
922 Oscillation, *J. Atmos. Sci.*, 75, 3753–3775, <https://doi.org/10.1175/JAS-D-18-0094.1>, 2018.
- 923 Kawatani, Y, Lee, J. N., and Hamilton, K.: Interannual variations of stratospheric water vapor in MLS
924 observations and climate model simulations, *J. Atmos. Sci.*, 71, 4072–4085,
925 <https://doi.org/10.1175/JAS-D-14-0164.1>, 2014.



- 926 Kawatani, Y., Hamilton, K., Sato, K., Dunkerton, T. J., Watanabe, S., and Kikuchi, K.: ENSO Modulation
927 of the QBO: Results from MIROC Models with and without Nonorographic Gravity Wave
928 Parameterization, *J. Atmos. Sci.*, 76, 3893–3917, <https://doi.org/10.1175/JAS-D-19-0163.1>, 2019.
- 929 Kelley, M., Schmidt, G. A., Nazarenko, L. S., Bauer, S. E., Ruedy, R., Russell, G. L., Ackerman, A. S.,
930 Aleinov, I., Bauer, M., Bleck, R., Canuto, V., Cesana, G., Cheng, Y., Clune, T. L., Cook, B. I., Cruz,
931 C. A., Del Genio, A. D., Elsaesser, G. S., Faluvegi, G., Kiang, N. Y., Kim, D., Lacis, A. A.,
932 Leboissetier, A., LeGrande, A. N., Lo, K. K., Marshall, J., Matthews, E. E., McDermid, S., Mezuman,
933 K., Miller, R. L., Murray, L. T., Oinas, V., Orbe, C., Pérez, C., García-Pando, C., Perlwitz, J. P.,
934 Puma, M. J., Rind, D., Romanou, A., Shindell, D. T., Sun, S., Tausnev, N., Tsigaridis, K., Tselioudis,
935 G., Weng, E., Wu, J., and Yao, M.-S.: GISS-E2.1: Configurations and climatology, *J. Adv. Model.*
936 *Earth Sy.*, 12, e2019MS002025, <https://doi.org/10.1029/2019MS002025>, 2020.
- 937 Labitzke, K.: On the interannual variability of the middle stratosphere during the northern winters, *J.*
938 *Meteorol. Soc. Jpn.*, 80, 963–971, http://doi.org/10.2151/jmsj1965.60.1_124, 1982.
- 939 Liess, S. and Geller, M. A.: On the relationship between QBO and distribution of tropical deep
940 convection, *J. Geophys. Res.*, 117, D03108, <http://dx.doi.org/10.1029/2011JD016317>, 2012.
- 941 Lindzen, R. S. and Holton, J. R.: A theory of the quasi-biennial oscillation, *J. Atmos. Sci.*, 25, 1095–
942 1107, [https://doi.org/10.1175/1520-0469\(1968\)025%3C1095:ATOTQB%3E2.0.CO;2](https://doi.org/10.1175/1520-0469(1968)025%3C1095:ATOTQB%3E2.0.CO;2), 1968.
- 943 Lott, F., Denvil, S., Butchart, N., Cagnazzo, C., Giorgetta, M. A., Hardiman, S. C., Manzini, E.,
944 Krismer, T., Duvel, J.-P., Maury, P., Scinocca, J. F., Watanabe, S., and Yukimoto, S.: Kelvin
945 and Rossby-gravity wave packets in the lower stratosphere of some high-top CMIP5 models, *J.*
946 *Geophys. Res.*, 119, 2156–2173, <https://doi.org/10.1002/2013JD020797>, 2014.



- 947 Maruyama, T. and Tsuneoka, Y.: Anomalously short duration of the QBO at 50 hPa of the easterly wind
948 phase in 1987 and its relationship to an El Niño event, *J. Meteorol. Soc. Jpn.*, 66, 629–634,
949 https://doi.org/10.2151/jmsj1965.66.4_629, 1988.
- 950 Miller, R. L., Schmidt, G. A., Nazarenko, L. S., Bauer, S. E., Kelley, M., Ruedy, R., Russell, G. L.,
951 Ackerman, A. S., Aleinov, I., Bauer, M., Bleck, R., Canuto, V., Cesana, G., Cheng, Y., Clune, T. L.,
952 Cook, B. I., Cruz, C. A., Del Genio, A. D., Elsaesser, G. S., Faluvegi, G., Kiang, N. Y., Kim, D.,
953 Lacis, A. A., Leboissetier, A., LeGrande, A. N., Lo, K. K., Marshall, J., Matthews, E. E., McDermid,
954 S., Mezuman, K., Murray, L. T., Oinas, V., Orbe, C., Pérez García-Pando, C., Perlwitz, J. P., Puma,
955 M. J., Rind, D., Romanou, A., Shindell, D. T., Sun, S., Tausnev, N., Tsigaridis, K., Tselioudis, G.,
956 Weng, E., Wu, J., and Yao, M. S.: CMIP6 Historical Simulations (1850–2014) With GISS-E2.1, *J.*
957 *Adv. Model. Earth Syst.*, 13, e2019MS002034, <https://doi.org/10.1029/2019MS002034>, 2021.
- 958 Moser, B. K. and Stevens, G. R.: Homogeneity of variance in the two-sample means test, *Am. Stat.*, 46,
959 19–21, <https://doi.org/10.1080/00031305.1992.10475839>, 1992.
- 960 Naujokat, B.: An update of the observed quasi-biennial oscillation of the stratospheric winds over the
961 tropics, *J. Atmos. Sci.*, 43, 1873–1877, [https://doi.org/10.1175/1520-0469\(1986\)043%3C1873:AUTOQ%3E2.0.CO;2](https://doi.org/10.1175/1520-0469(1986)043%3C1873:AUTOQ%3E2.0.CO;2), 1986.
- 963 Nazarenko, L. S., Tausnev, N., Russell, G. L., Rind, D., Miller, R. L., Schmidt, G. A., Bauer, S. E., Kelley,
964 M., Ruedy, R., Ackerman, A. S., Aleinov, I., Bauer, M., Bleck, R., Canuto, V., Cesana, G., Cheng,
965 Y., Clune, T. L., Cook, B. I., Cruz, C. A., Del Genio, A. D., Elsaesser, G. S., Faluvegi, G., Kiang, N.
966 Y., Kim, D., Lacis, A. A., Leboissetier, A., LeGrande, A. N., Lo, K. K., Marshall, J., Matthews, E.
967 E., McDermid, S., Mezuman, K., Murray, L. T., Oinas, V., Orbe, C., Pérez García-Pando, C.,
968 Perlwitz, J. P., Puma, M. J., Romanou, A., Shindell, D. T., Sun, S., Tsigaridis, K., Tselioudis, G.,
969 Weng, E., Wu, J., and Yao, M.-S.: Future Climate Change Under SSP Emission Scenarios With



970 GISS-E2.1, J. Adv. Model. Earth Syst., 14,
971 e2021MS002871, <https://doi.org/10.1029/2021MS002871>, 2022.

972 Oort, A. H. and Yienger, J. J.: Observed interannual variability in the Hadley circulation and its
973 connection to ENSO, J. Climate, 9, 2751–2767, [https://doi.org/10.1175/1520-0442\(1996\)009<2751:Oivith>2.0.Co;2](https://doi.org/10.1175/1520-0442(1996)009<2751:Oivith>2.0.Co;2), 1996.

975 Orbe, C., Rind, D., Jonas, J., Nazarenko, L., Faluvegi, G., Murray, L.T., Shindell, D.T., Tsigaridis, K.,
976 Zhou, T., Kelley, M., and Schmidt, G.: GISS Model E2.2: A climate model optimized for the middle
977 atmosphere. Part 2: Validation of large-scale transport and evaluation of climate response, *J.*
978 *Geophys. Res. Atmos.*, 125, e2020JD033151, <https://doi.org/10.1029/2020JD033151>, 2020.

979 Philander, S. G. H.: El Niño, La Niña, and the Southern Oscillation, Academic Press, San Diego, 293pp.,
980 1990.

981 Plumb, R. A.: The interaction of two internal waves with the mean flow: Implications for the theory of
982 the quasi-biennial oscillation, J. Atmos. Sci., 34, 1847–1858, [https://doi.org/10.1175/1520-0469\(1977\)034<1847:TIOTIW>2.0.CO;2](https://doi.org/10.1175/1520-0469(1977)034<1847:TIOTIW>2.0.CO;2), 1977.

984 Rayner, N. A., Parker, D. E., Horton, E. B., Folland, C. K., Alexander, L. V., Rowell, D. P., Kent, E. C.,
985 and Kaplan, A.: Global analyses of sea surface temperature, sea ice, and night marine air temperature
986 since the late nineteenth century, J. Geophys. Res., 108, 4407,
987 <https://doi.org/10.1029/2002JD002670>, 2003.

988 Richter, J. H., Solomon, A., and Bacmeister, J. T.: On the simulation of the quasi-biennial oscillation in
989 the Community Atmosphere Model, version 5, J. Geophys. Res.-Atmos., 119, 3045–
990 3062, <https://doi.org/10.1002/2013JD021122>, 2014.



- 991 Richter, J. H., Anstey, J. A., Butchart, N., Kawatani, Y., Meehl, G. A., Osprey, S., and Simpson, I. R.:
992 Progress in simulating the quasi-biennial oscillation in CMIP models, *J. Geophys. Res.-Atmos.*, 125,
993 e2019JD032362, <https://doi.org/10.1029/2019JD032362>, 2020.
- 994 Rind, D., Suozzo, R., Balachandran, N. K., Lacis, A., and Russell, G.: The GISS global climate-middle
995 atmosphere model. Part I: Model structure and climatology, *J. Atmos. Sci.*, 45, 329–370,
996 [https://doi.org/10.1175/1520-0469\(1988\)045%3C0329:TGGCMA%3E2.0.CO;2](https://doi.org/10.1175/1520-0469(1988)045%3C0329:TGGCMA%3E2.0.CO;2), 1988.
- 997 Rind, D., Jonas, J., Balachandran, N., Schmidt, G., and Lean, J.: The QBO in two GISS global climate
998 models: 1. Generation of the QBO, *J. Geophys. Res. Atmos.*, 119, 8798–8824,
999 <https://doi.org/10.1002/2014JD021678>, 2014.
- 1000 Rind, D., Orbe, C., Jonas, J., Nazarenko, L., Zhou, T., Kelley, M., Lacis, A., Shindell, D., Faluvegi,
1001 Russell, G., Bauer, M., Schmidt, G., Romanou, A., and Tausnev, N.: GISS Model E2.2: A climate
1002 model optimized for the middle atmosphere — Model structure, climatology, variability and climate
1003 sensitivity, *J. Geophys. Res. Atmos.*, 125, e2019JD032204, <https://doi.org/10.1029/2019JD032204>,
1004 2020.
- 1005 Salby, M. and Garcia, R.: Transient response to localized episodic heating in the tropics, Part 1: excitation
1006 and short-time near-field behavior, *J. Atmos. Sci.*, 44, 458–498, [https://doi.org/10.1175/1520-0469\(1987\)044%3C0458:TRTLEH%3E2.0.CO;2](https://doi.org/10.1175/1520-0469(1987)044%3C0458:TRTLEH%3E2.0.CO;2), 1987.
- 1008 Scaife, A. A., Butchart, N., Warner, C. D., Stainforth, D., Norton, W., and Austin, J.: Realistic quasi-
1009 biennial oscillations in a simulation of the global climate, *Geophys. Res. Lett.*, 27, 3481–3484,
1010 <https://doi.org/10.1029/2000GL011625>, 2000.
- 1011 Schirber, S., Manzini, E., Krismer, T. and Giorgetta, M.: The Quasi-Biennial Oscillation in a warmer
1012 climate: sensitivity to different gravity wave parameterizations, *Climate Dynamics*, 45, 825–
1013 836, <https://doi.org/10.1007/s00382-014-2314-2>, 2015.



- 1014 Schmidt, G. A., Kelley, M., Nazarenko, L., Ruedy, R., Russell, G. L., Aleinov, I., Bauer, M., Bauer, S.
1015 E., Bhat, M. K., Bleck, R., Canuto, V., Chen, Y.-H., Cheng, Y., Clune, T. L., Del Genio, A., de
1016 Fainchtein, R., Faluvegi, G., Hansen, J. E., Healy, R. J., Kiang, N. Y., Koch, D., Lacis, A. A.,
1017 LeGrande, A. N., Lerner, J., Lo, K. K., Matthews, E. E., Menon, S., Miller, R. L., Oinas, V.,
1018 Oloso, A. O., Perlwitz, J. P., Puma, M. J., Putman, W. M., Rind, D., Romanou, A., Sato, M.,
1019 Shindell, D. T., Sun, S., Syed, R. A., Tausnev, N., Tsigaridis, K., Unger, N., Voulgarakis, A.,
1020 Yao, M.-S., and Zhang, J.: Configuration and assessment of the GISS ModelE2 contributions to
1021 the CMIP5 archive, *J. Adv. Model. Earth Syst.*, 6, 141–
1022 184, <https://doi.org/10.1002/2013MS000265>, 2014
- 1023 Serva, F., Cagnazzo, C., Christiansen, B., and Yang, S.: The influence of ENSO events on the
1024 stratospheric QBO in a multi-model ensemble, *Climate Dynamics*, 54, 2561–2575,
1025 <https://doi.org/10.1007/s00382-020-05131-7>, 2020.
- 1026 Simpson, I. R., Shepherd, T. G., and Sigmond, M.: Dynamics of the lower stratospheric circulation
1027 response to ENSO, *J. Atmos. Sci.*, 68, 2537–2556, <https://doi.org/10.1175/JAS-D-11-05.1>, 2011.
- 1028 Sullivan, S. C., Schiro, K. A., Stubenrauch, C., and Gentine, P.: The response of tropical organized
1029 convection to El Niño warming, *J. Geophys. Res.-Atmos.*, 124, 8481–
1030 8500, <https://doi.org/10.1029/2019JD031026>, 2019.
- 1031 Trepte, C. R. and Hitchman, M. H.: Tropical stratospheric circulation deduced from satellite aerosol data,
1032 *Nature*, 355, 626–628, <https://doi.org/10.1038/355626a0>, 1992.
- 1033 Tsuda, T., Ratnam, M. V., Alexander, S. P., Kozu, T., and Takayabu, Y.: Temporal and spatial
1034 distributions of atmospheric wave energy in the equatorial stratosphere revealed by GPS radio
1035 occultation temperature data obtained with the CHAMP Satellite during 2001–2006, *Earth Planets
1036 Space*, 61, 525–533, <https://doi.org/10.1186/BF03353169>, 2009.



- 1037 Wallace, J., Panetta, R., and Estberg, J.: Representation of the equatorial stratospheric quasi- biennial
1038 oscillation in EOF phase space, *J. Atmos. Sci.*, 50, 1751–1762, [https://doi.org/10.1175/1520-](https://doi.org/10.1175/1520-0469(1993)050<1751:ROTESQ>2.0.CO;2)
1039 [0469\(1993\)050<1751:ROTESQ>2.0.CO;2](https://doi.org/10.1175/1520-0469(1993)050<1751:ROTESQ>2.0.CO;2), 1993.
- 1040 Wang, C., Deser, C., Yu, J.-Y., DiNezio, P., and Clement, A.: El Niño–Southern Oscillation (ENSO): A
1041 review. In *Reefs of the Eastern Pacific*, Springer Sci. Publish., 85–106, [https://doi.org/10.1007/978-](https://doi.org/10.1007/978-94-017-7499-4_4)
1042 [94-017-7499-4_4](https://doi.org/10.1007/978-94-017-7499-4_4), 2016.
- 1043 Xu, J.-S., On the relationship between the stratospheric quasi-biennial oscillation and the tropospheric
1044 southern oscillation, *J. Atmos. Sci.*, 49, 725–734, [https://doi.org/10.1175/1520-](https://doi.org/10.1175/1520-0469(1992)049<0725:OTRBTS>2.0.CO;2)
1045 [0469\(1992\)049<0725:OTRBTS>2.0.CO;2](https://doi.org/10.1175/1520-0469(1992)049<0725:OTRBTS>2.0.CO;2), 1992.
- 1046 Yoo, C. and Son, S.-W.: Modulation of the boreal wintertime Madden-Julian oscillation by the
1047 stratospheric quasi-biennial oscillation, *Geophys. Res. Lett.*, 43, 1392–1398,
1048 <https://doi.org/10.1002/2016GL067762>, 2016.
- 1049 Yu, J.-Y. and Mechoso, C. R.: A coupled atmosphere–ocean GCM study of the ENSO, *J. Climate*,
1050 14, 2329–2350, [https://doi.org/10.1175/1520-0442\(2001\)014%3C2329:ACAOGS%3E2.0.CO;2](https://doi.org/10.1175/1520-0442(2001)014%3C2329:ACAOGS%3E2.0.CO;2),
1051 2001.
- 1052 Yuan, W., Geller, M. A., and Love, P. T.: ENSO influence on QBO modulations of the tropical
1053 tropopause, *Q. J. Roy. Meteorol. Soc.*, 140, 1670–1676, <https://doi.org/10.1002/qj.2247>, 2014.
- 1054 Zawodny, J. M. and McCormick, M. P.: Stratospheric Aerosol and Gas Experiment II measurements of
1055 the quasi-biennial oscillations in ozone and nitrogen dioxide, *J. Geophys. Res.*, 96, 9371– 9377,
1056 <http://dx.doi.org/10.1029/91JD00517>, 1991.
- 1057 Zhao, Y. and Sun, D.-Z.: ENSO asymmetry in CMIP6 models, *J. Climate*, 5555–5572,
1058 <https://doi.org/10.1175/JCLI-D-21-0835.1>, 2022.



1059 Zhang, C.: Large-scale variability of atmospheric deep convection in relation to sea surface temperature

1060 in the tropics, *J. Climate*, 6, 1898–1913, <https://doi.org/10.1175/1520->

1061 [0442\(1993\)006<1898:LSVOAD>2.0.CO;2](https://doi.org/10.1175/1520-0442(1993)006<1898:LSVOAD>2.0.CO;2), 1993.

1062



Table 1 The model configurations and respective ensemble simulations

Model configuration	Simulation	CMIP6 archive tag	Period	Ensemble size	Ensemble name
AMIP-OMA-SP	Historical AMIP	N/A	1850–2014	5	E1
AMIP-OMA-AP	Historical AMIP	N/A*	1850–2014	4	E2
Coupled-NINT-SP	CMIP6 Historical	N/A#	1850–2014	5	E3
Coupled-NINT-AP	CMIP6 Historical	E2-2-G.historical.r[1-5]i1p1f1	1850–2014	5	E4
Coupled-OMA-AP	CMIP6 Historical	E2-2-G.historical.r[1-5]i1p3f1	1850–2014	5	E5

*E2-2-G.amip.r[1-5]i1p3f1 in the CMIP6 archive are the outputs of the same model, but range from 1979 to 2014.

Coupled-NINT-SP outputs follow the CMIP6 protocol and naming. Four of five runs are available from NCCS portal at https://portal.nccs.nasa.gov/datashare/giss_cmip6/CMIP/NASA-GISS/GISS-E2.2.1-G/

1063

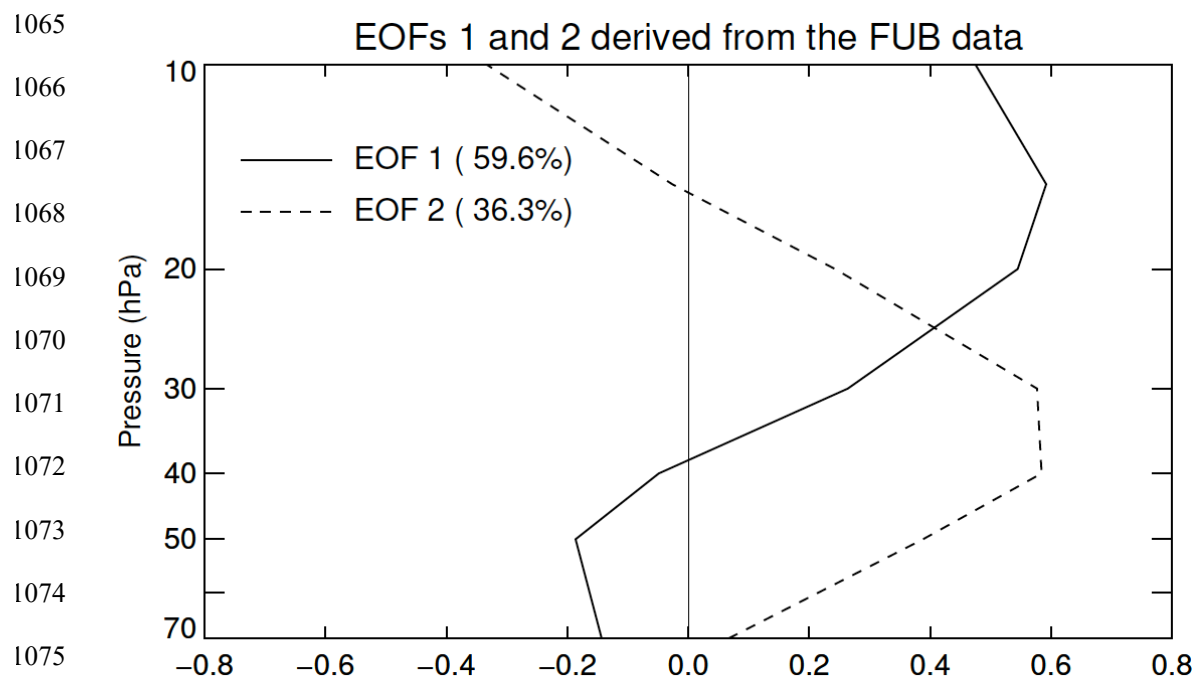


Table 2 The ENSO influence on the QBO period

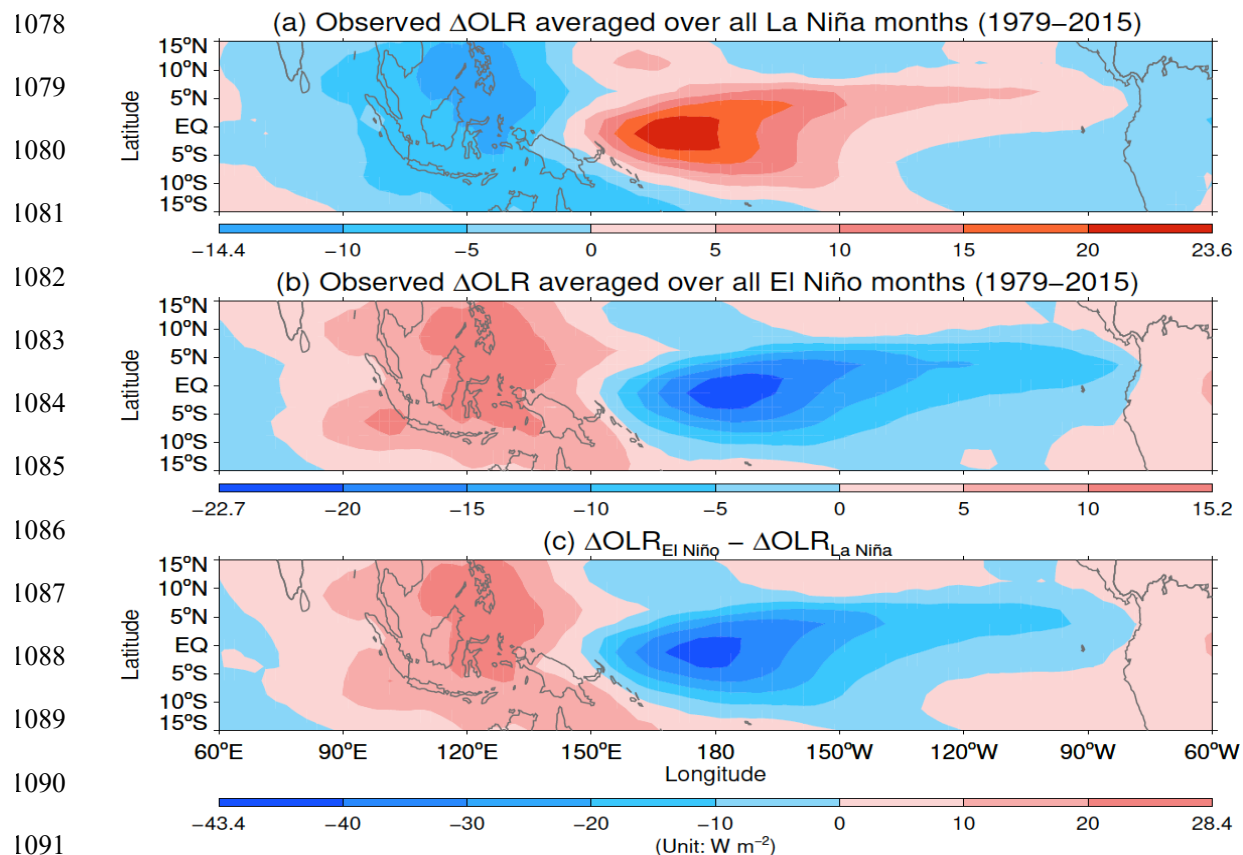
Member		r1			r2			r3			r4			r5		
ENSO Phase		EL	LA	EL-LA	EL	LA	EL-LA	EL	LA	EL-LA	EL	LA	EL-LA	EL	LA	EL-LA
Period (month)	E1	31.1	34.0	-2.9	34.9	35.9	-1.0	29.4	32.9	-3.5	29.7	36.7	-7.0	30.5	35.7	-5.2
	E2	33.1	36.5	-3.4	31.5	35.6	-4.1	32.1	35.4	-3.2	29.4	36.8	-7.4	n/a	n/a	n/a
	E3	27.5	33.7	-6.2	28.0	30.5	-2.5	30.5	29.8	0.7	30.0	31.5	-1.5	28.2	32.0	-3.8
	E4	31.2	35.0	-3.8	29.8	32.4	-2.6	29.7	35.4	-5.7	28.0	34.7	-6.7	28.0	33.4	-5.4
	E5	32.6	38.6	-6.0	33.0	37.8	-4.8	33.0	38.0	-5.0	32.3	39.2	-6.9	32.3	37.6	-5.3

E[1-5] denote the ensemble simulations AMIP-OMA, AMIP-OMA-AP, Coupled-NINT-SP, Coupled-NINT-AP, and Coupled-OMA-AP, respectively. r[1-5] indicate the ensemble members of those simulations. EL and LA are short for El Niño than during La Niña, respectively. The red and bold numbers can be regarded as being statistically significantly different from zero at the 5% significance level.

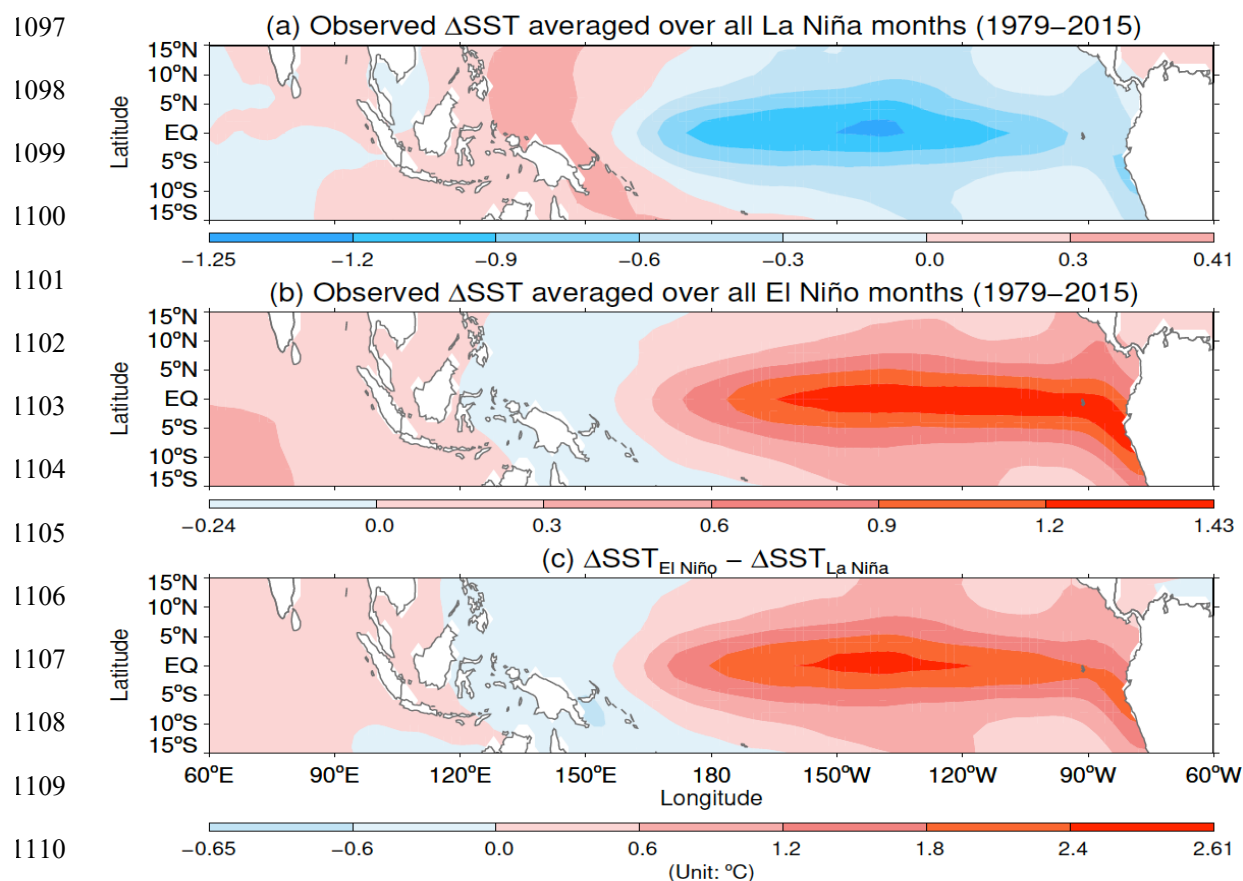
1064



1076 **Fig. 1.** The first (solid line) and second (dashed line) orthonormal eigenvectors derived from the
1077 deseasonalized and smoothed FUB zonal winds between 1953 and 2015.



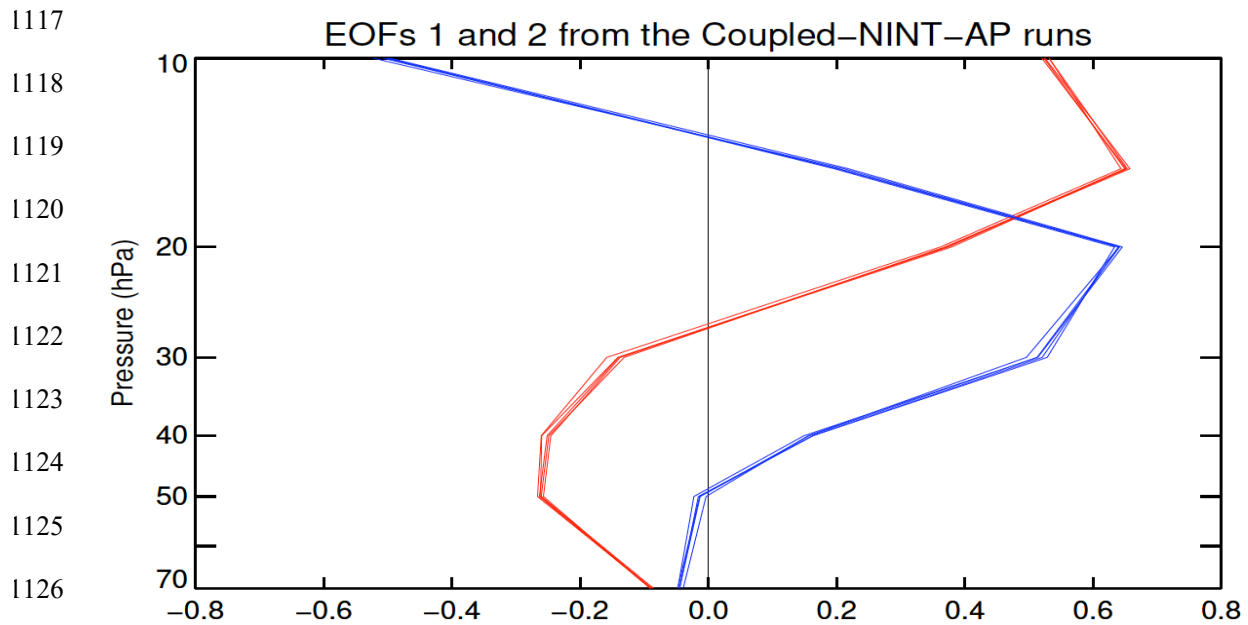
1092 **Fig. 2.** Mean OLR deviations from climatology for (a) La Niña and (b) El Niño conditions over the
1093 tropical Indian and Pacific oceans. (c) Differences of mean OLR anomalies between El Niño and La Niña
1094 conditions. The mean composite OLR anomalies and their differences are derived from the datasets
1095 provided by NOAA NCEI.
1096



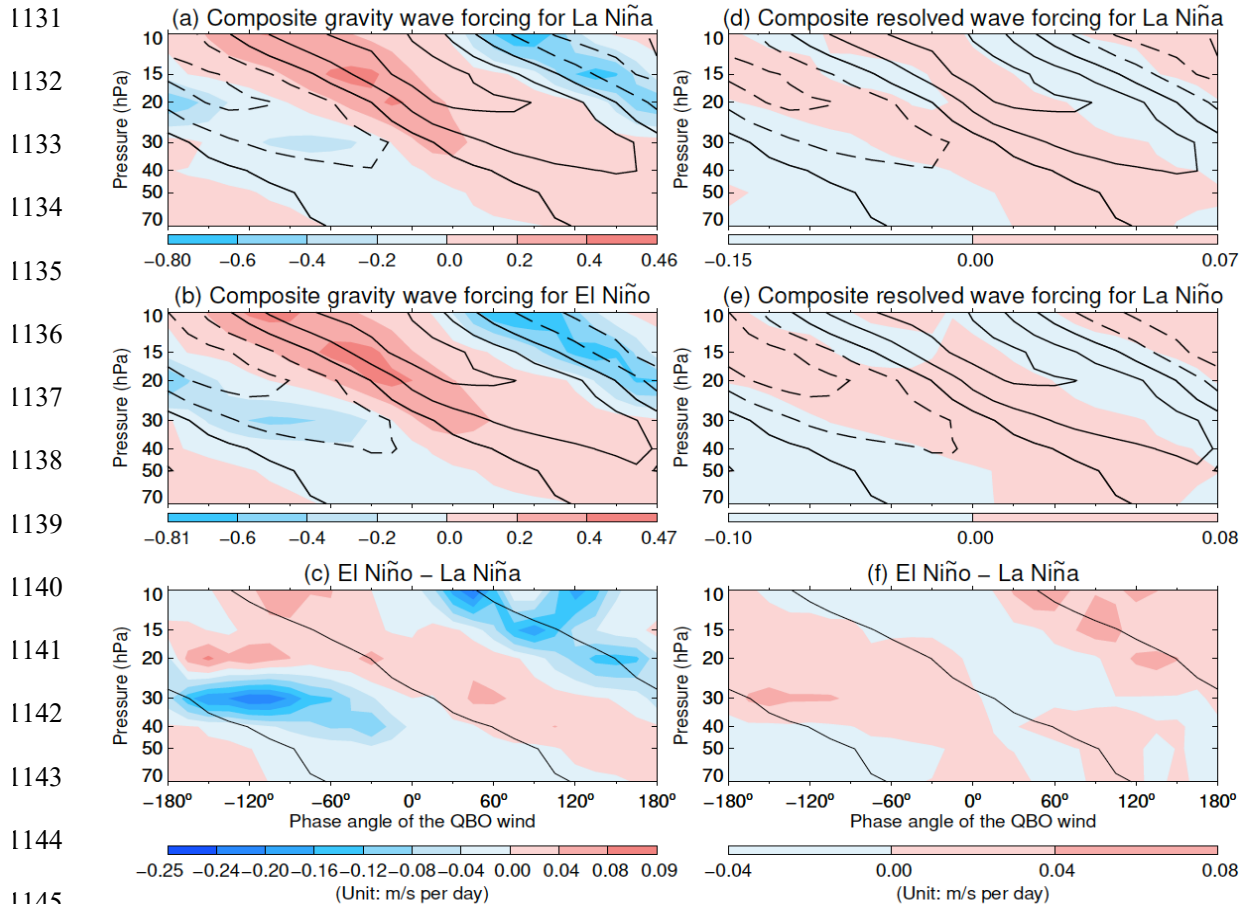
1111 **Fig. 3.** Mean SST deviations from climatology for (a) La Niña and (b) El Niño conditions over the tropical
1112 Indian and Pacific oceans. (c) Differences of mean SST anomalies between El Niño and La Niña
1113 conditions. The mean composite SST anomalies and their differences are derived from the NOAA
1114 ERSSTv5 SST.

1115

1116

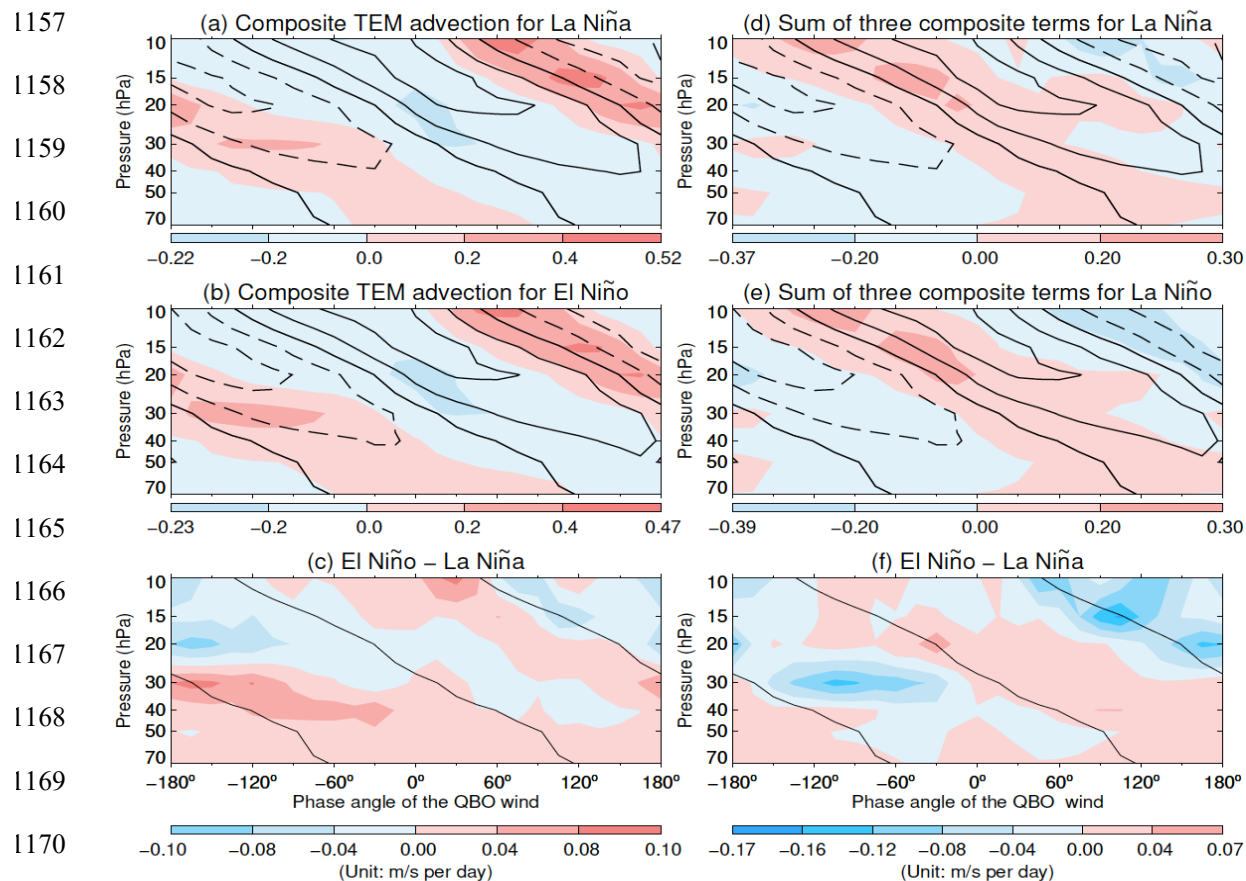


1127 **Fig. 4.** The first (red lines) and second (blue lines) orthonormal eigenvectors derived from the
1128 deseasonalized and smoothed equatorial zonal mean zonal winds between 1873 and 2013 from the five
1129 Coupled–NINT–AP runs.
1130



1146 **Fig. 5.** Ensemble average of the composite QBO winds simulated by the Coupled–NINT–AP model
1147 during La Niña (upper panels) and El Niño (middle panels) is depicted by black contour lines where the
1148 contour interval is 10 m s^{-1} with dashed lines denoting negatives and solid lines denoting positives and
1149 zero. The location of strong shear zones of the QBO winds during ENSO extremes is delineated by the
1150 zero wind contour lines in lower panels. For color filled contours, left panels depict the ensemble average
1151 of the composite gravity wave forcing simulated by the Coupled–NINT–AP model averaged from 5°S to
1152 5°N during La Niña (a) and El Niño (b) and its composite difference between El Niño and La Niña (c);
1153 right panels depict the ensemble average of the composite resolved wave forcing simulated by the
1154 Coupled–NINT–AP model during La Niña (d) and El Niño (e) and its composite difference between El
1155 Niño and La Niña (f).

1156



1171 **Fig. 6.** The black contour lines are the same as those in Fig. 5. For color filled contours, left panels depict
 1172 the ensemble average of the composite TEM advection simulated by the Coupled–NINT–AP model
 1173 averaged from 5°S to 5°N during La Niña (a) and El Niño (b) and the composite difference between El
 1174 Niño and La Niña (c); right panels depict the ensemble mean totaling of the composite fields of gravity
 1175 wave forcing, resolved wave forcing, and TEM advection simulated by the Coupled–NINT–AP model
 1176 during La Niña (d) and El Niño (e) and the composite difference between El Niño and La Niña (f).
 1177

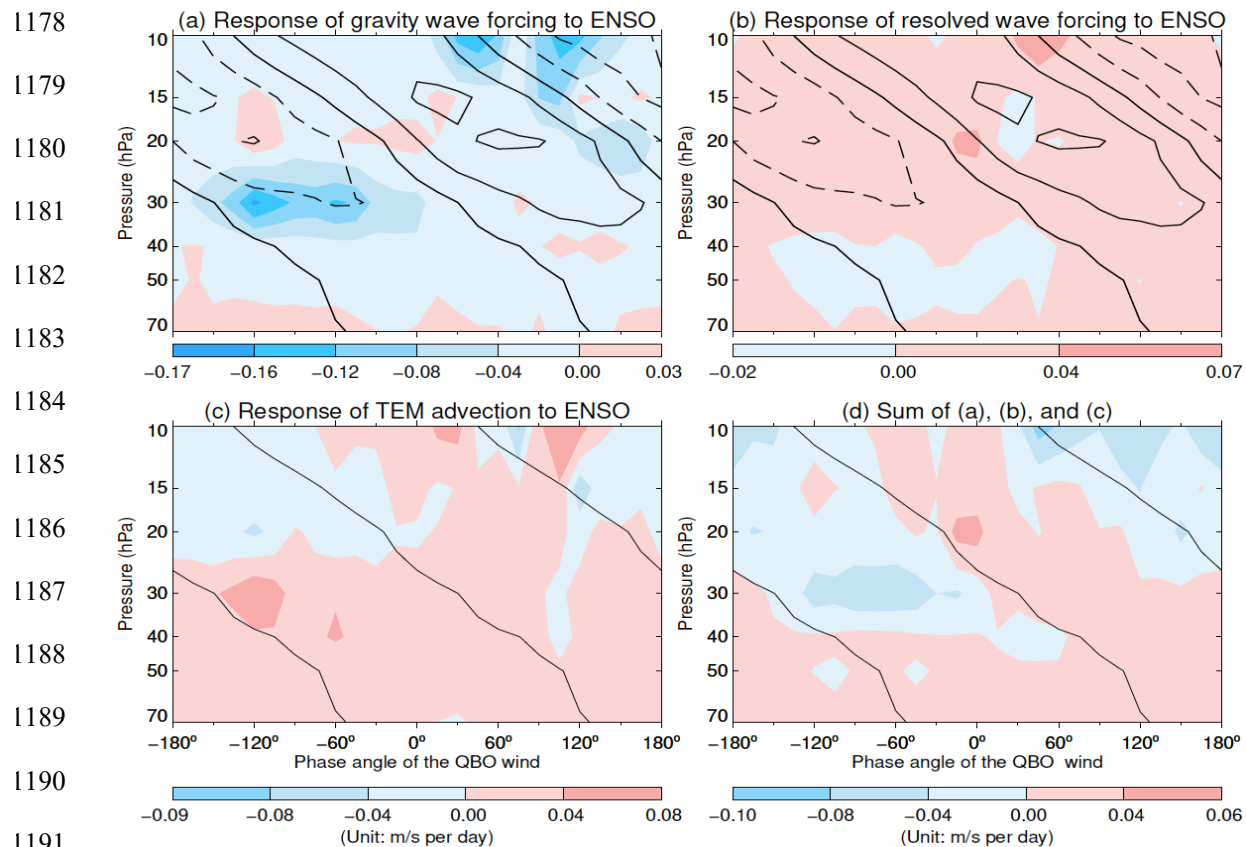
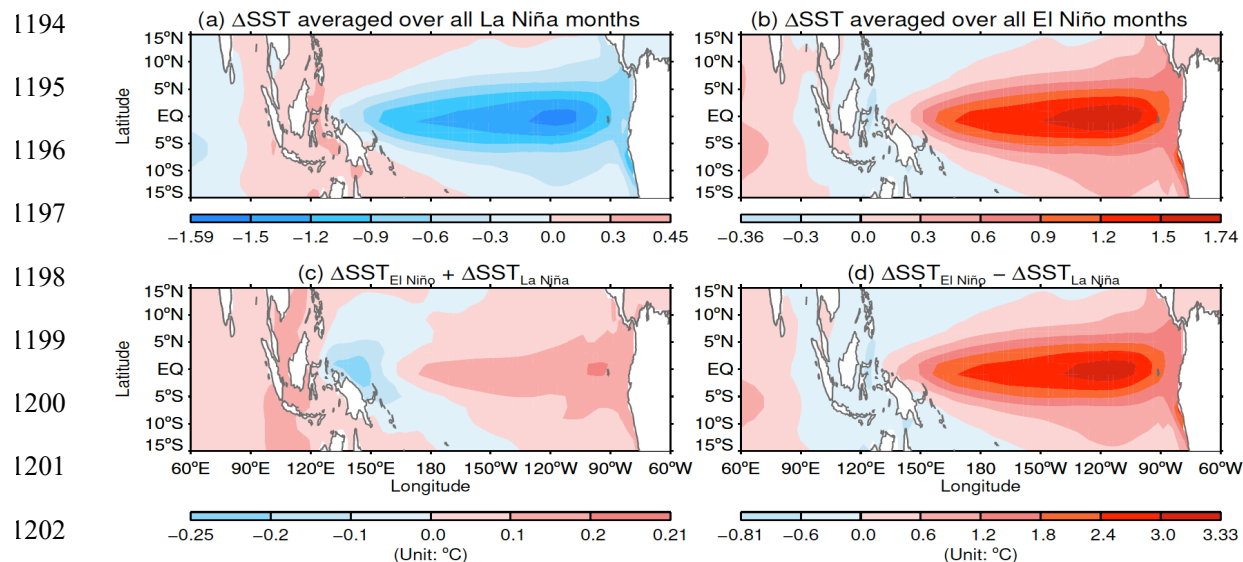
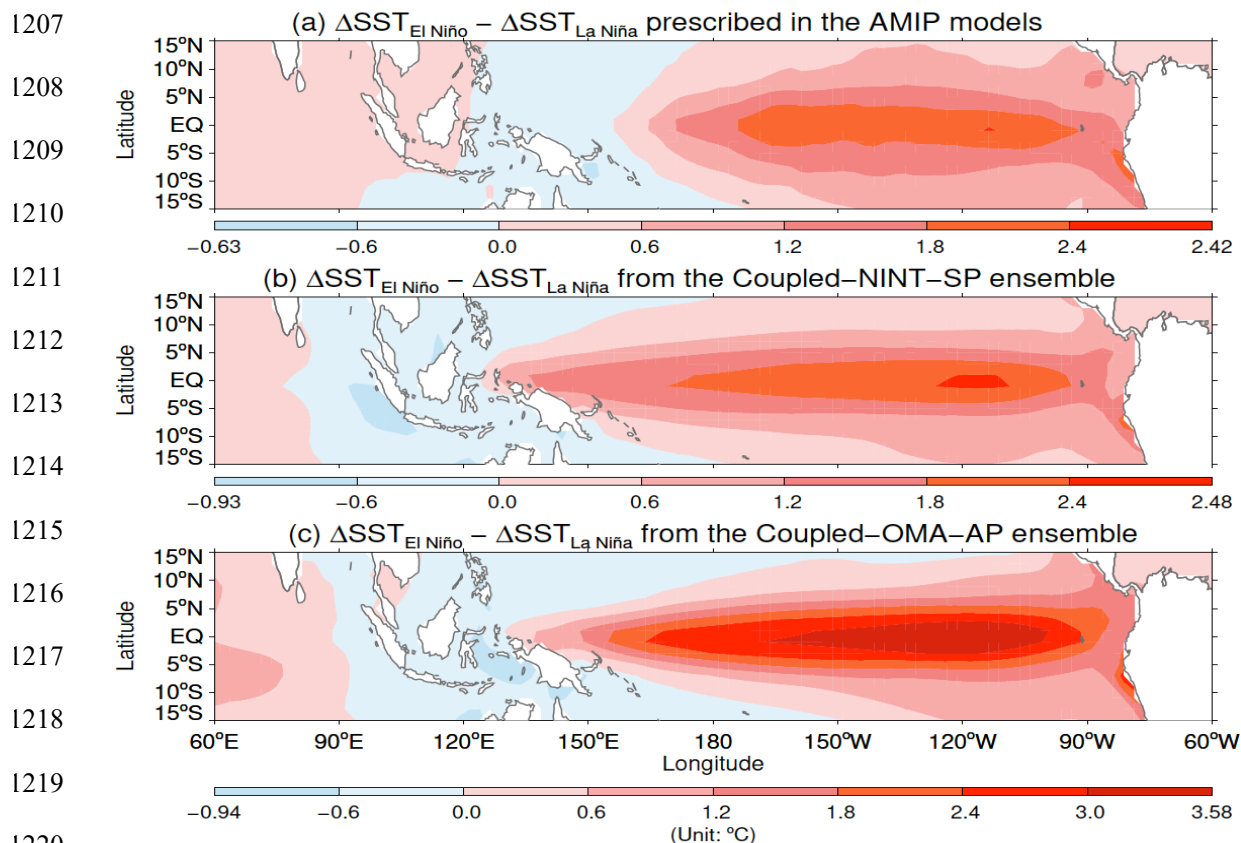


Fig. 7. (a) and (b) are the same as the bottom panels in Fig. 5 except for the Coupled-NINT-SP model. (c) and (d) are the same as the bottom panels in Fig. 6 except for the Coupled-NINT-SP model.

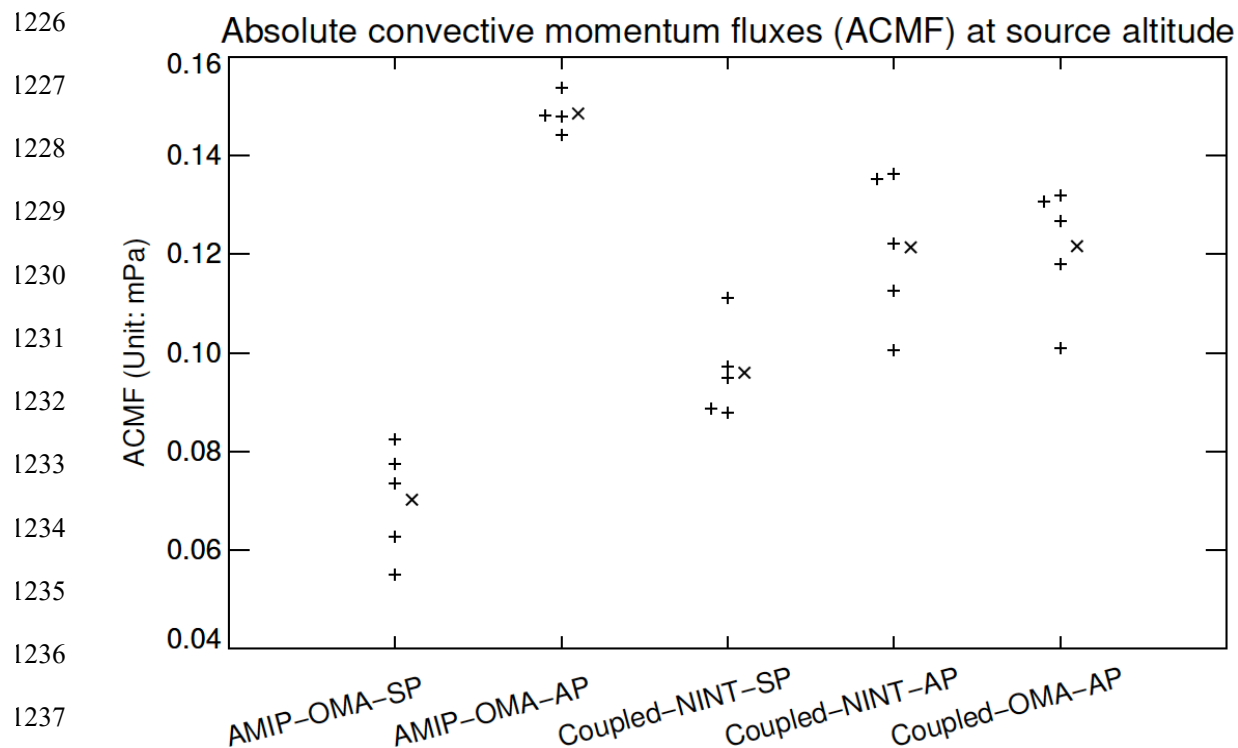


1203 **Fig. 8.** Ensemble mean of the composite SST anomalies averaged over all La Niña (a) and El Niño (b)
1204 months respectively over the 1871–2013 period, their sum (c) and difference (d) simulated by the
1205 Coupled-NINT-AP model.
1206

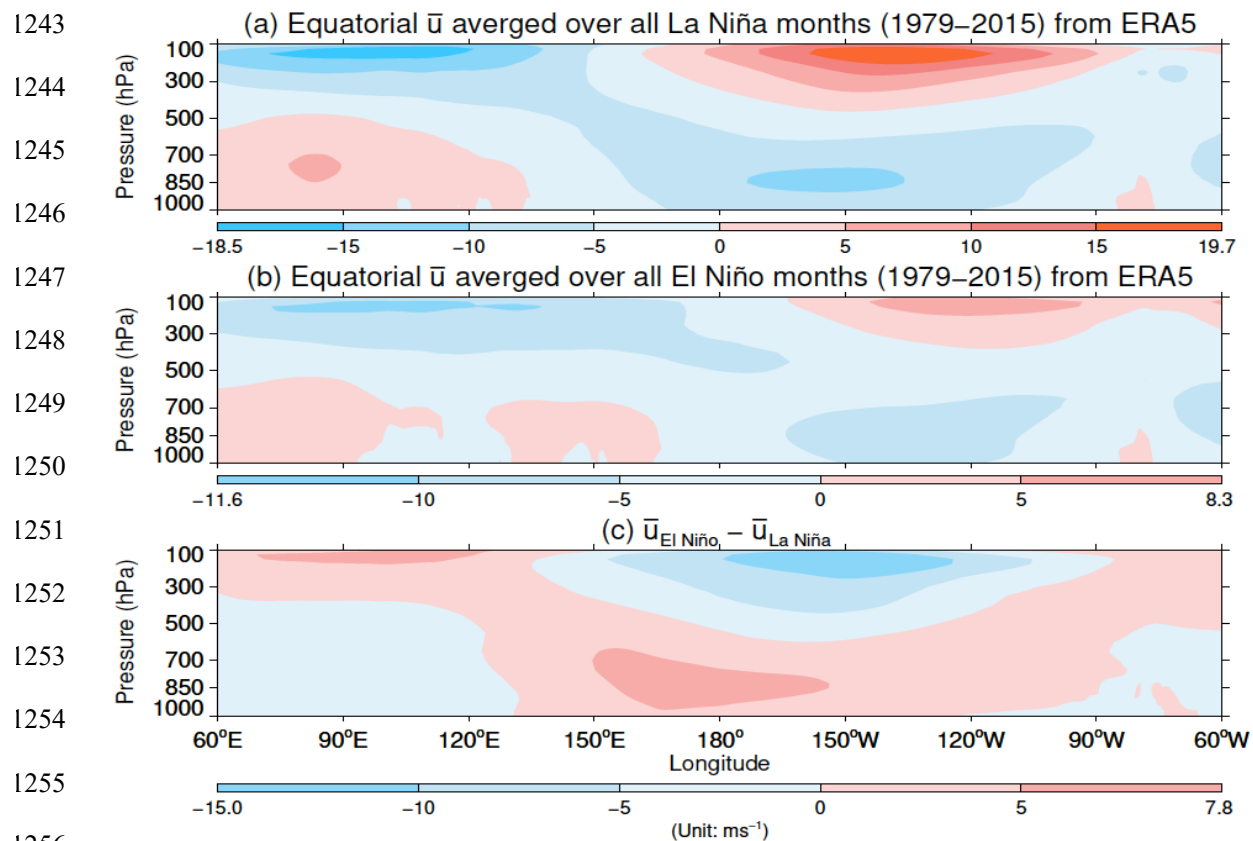


1221 **Fig. 9.** Difference in the composite SST anomalies between El Niño and La Niña over the 1871–2013
1222 period specified in the AMIP-OMA-SP and AMIP-OMA-AP models (a) and ensemble mean difference
1223 in the composite SST anomalies between El Niño and La Niña over the 1871–2013 period simulated by
1224 the Coupled-NINT-SP (b) and Coupled-OMA-AP (c) models.

1225



1238 **Fig. 10.** Difference in the composite ACMF anomalies at the source altitude averaged over the 5°S – 5°N
 1239 latitudinal belt between El Niño and La Niña over the 1871–2013 period. Plus symbol (+) denotes the
 1240 difference from individual runs while cross symbol (x) represents each ensemble mean difference. Some
 1241 symbols are slightly shifted leftward or rightward to avoid overlapping with other symbols.
 1242



1257 **Fig. 11.** Zonal winds from ERA5 averaged from 5°S to 5°N that are further averaged over all La Niña (a)

1258 and El Niño (b) months between 1979 and 2015 respectively, and their differences (c).

1259



1260

1261

1262

1263

1264

1265

1266

1267

1268

1269

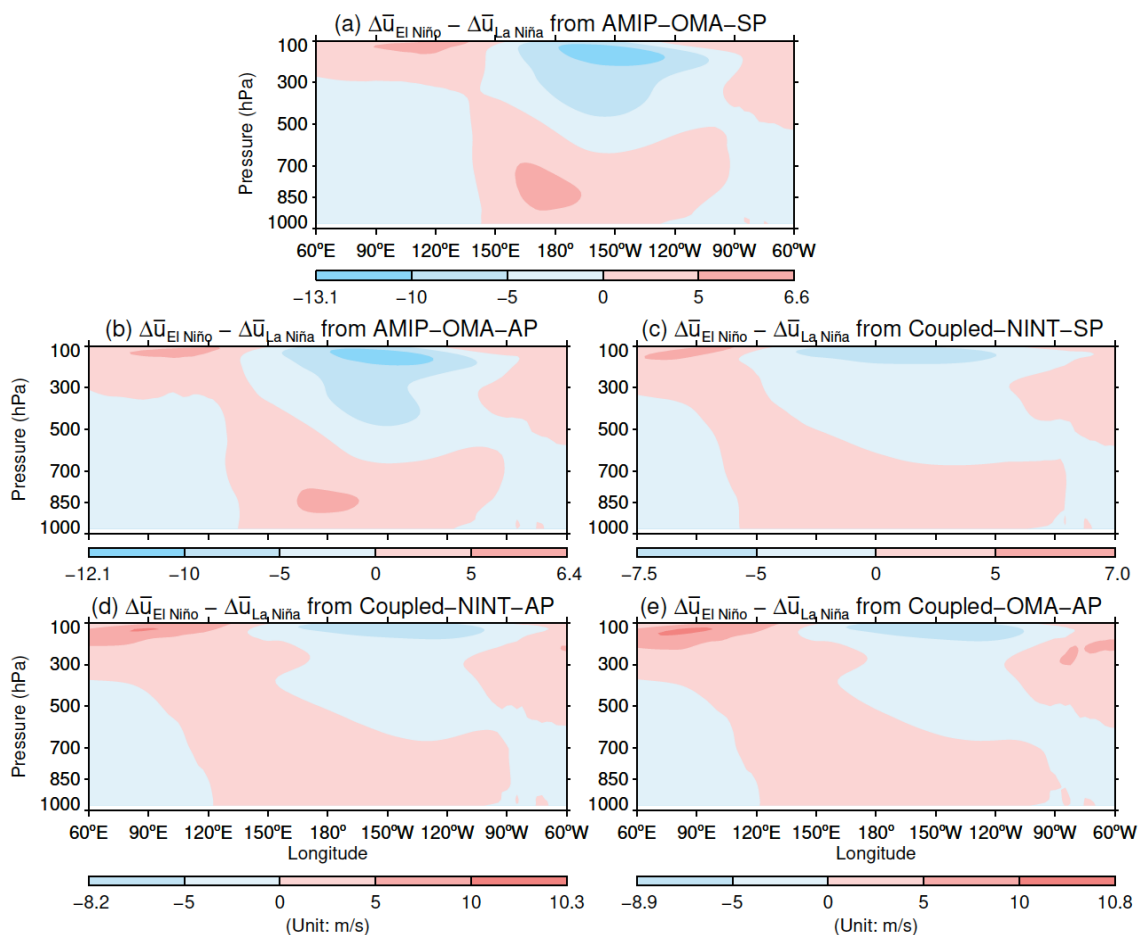
1270

1271

1272

1273

1274



1275

1276

1277

1278

Fig. 12. Same as Fig. 11c but for the ensemble averages of the composite difference in zonal wind anomalies between El Niño and La Niña simulated by AMIP-OMA-SP (a), AMIP-OMA-AP (b), Coupled-NINT-SP (c), Coupled-NINT-AP (d), and Coupled-OMA-AP (e).



1279

1280

1281

1282

1283

1284

1285

1286

1287

1288

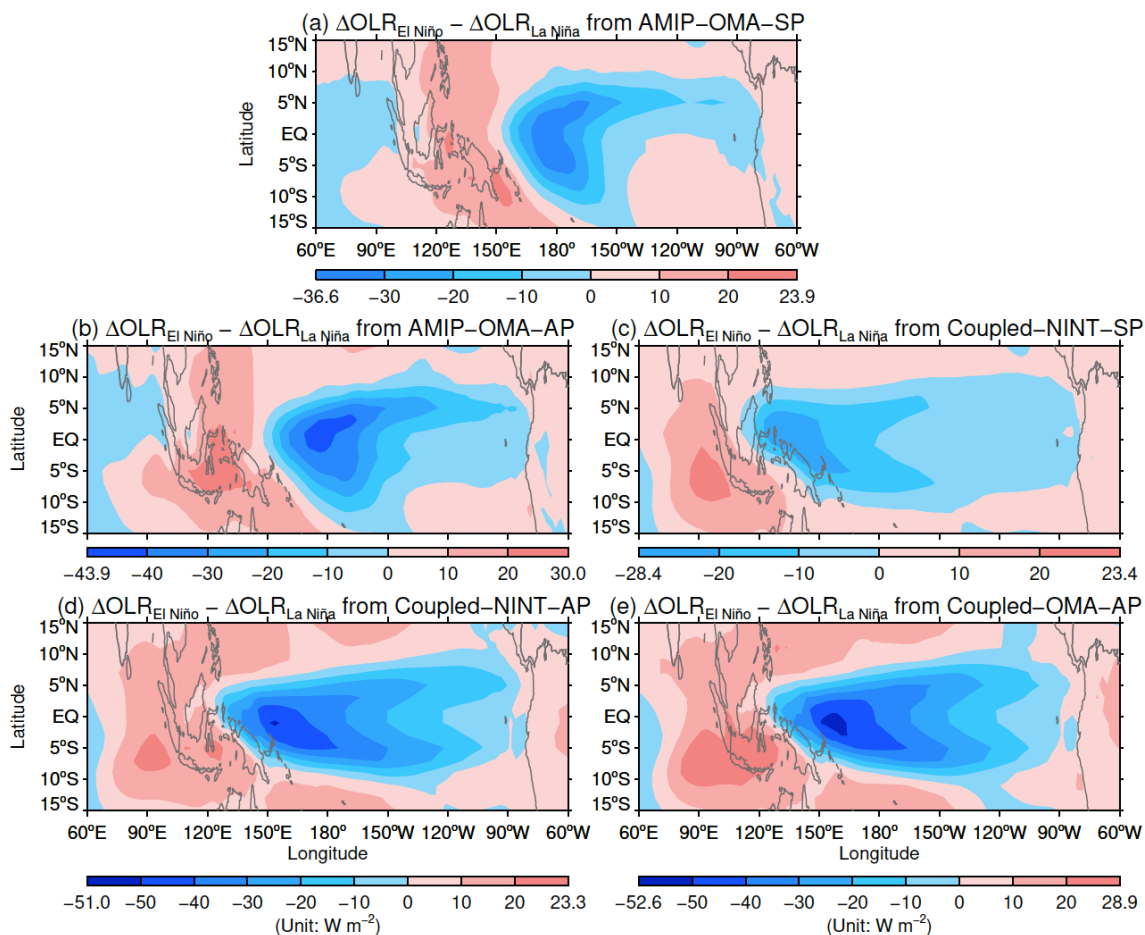
1289

1290

1291

1292

1293



1294

Fig. 13. Same as Fig. 12 but for the ensemble averages of the composite difference in OLR anomalies between El Niño and La Niña simulated by AMIP-OMA-SP (a), AMIP-OMA-AP (b), Coupled-NINT-SP (c), Coupled-NINT-AP (d), and Coupled-OMA-AP (e).

1297



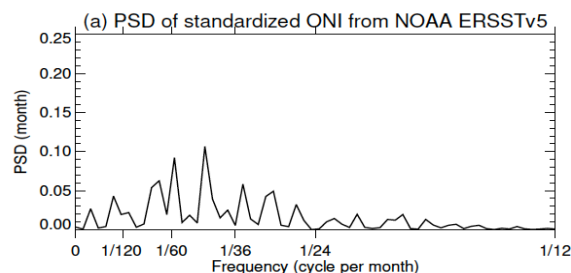
1298

1299

1300

1301

1302

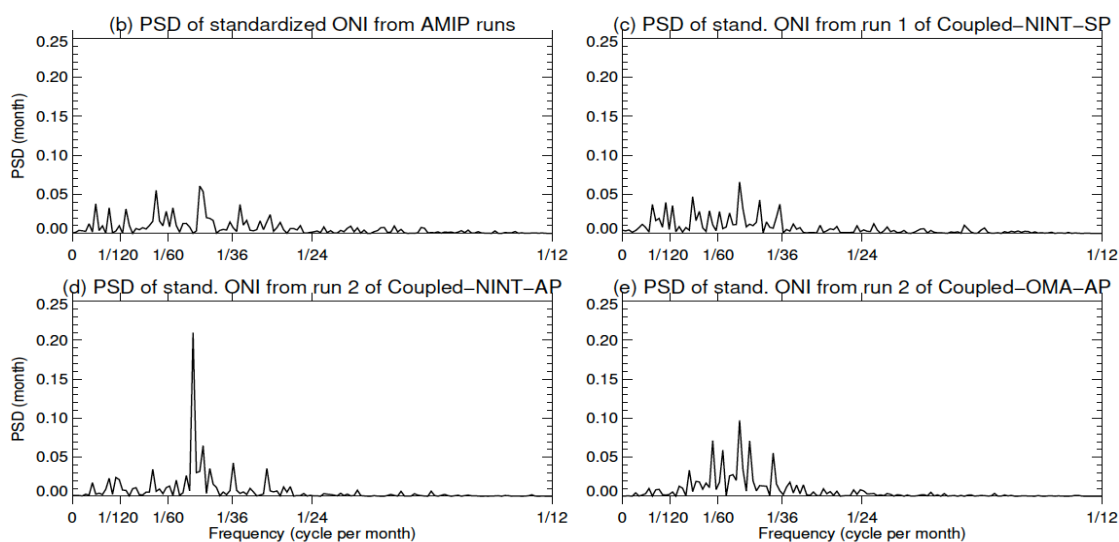


1303

1304

1305

1306



1307

1308

1309

1310

1311

Fig. 14. Power spectral densities (PSD) of the standardized ONI between 1953 and 2015 derived from the NOAA ERSSTv5 SST (a), of standardized ONI between 1871 and 2013 derived from the HadISST1 dataset (b), of standardized ONI between 1871 and 2013 simulated by the first realization of Coupled-NINT-SP (c), and of those from the second realizations of Coupled-NINT-AP (d) and Coupled-OMA-AP (e).

1316